



Virginia Commonwealth University  
**VCU Scholars Compass**

---

Theses and Dissertations

Graduate School

---

2023

## KPT-330 synergizes with everolimus to reduce mTORC1-overactive basal-like triple-negative breast cancer brain metastasis burden

Aaron D. Valentine  
*Virginia Commonwealth University*

Follow this and additional works at: <https://scholarscompass.vcu.edu/etd>



Part of the [Cancer Biology Commons](#)

© Aaron D. Valentine 2023

---

**Downloaded from**

<https://scholarscompass.vcu.edu/etd/7448>

This Thesis is brought to you for free and open access by the Graduate School at VCU Scholars Compass. It has been accepted for inclusion in Theses and Dissertations by an authorized administrator of VCU Scholars Compass. For more information, please contact [libcompass@vcu.edu](mailto:libcompass@vcu.edu).

# **KPT-330 synergizes with everolimus to reduce mTORC1-overactive basal-like triple-negative breast cancer brain metastasis burden**

A thesis submitted in partial fulfillment of the requirements for the degree of Master of  
Science at Virginia Commonwealth University.

By

**Aaron David Valentine**

Bachelor of Science, Jacobs University Bremen, 2021

Director: J. Chuck Harrell, PhD

Associate Professor

Department of Pathology

Virginia Commonwealth University

Richmond, Virginia

July 2023

## Acknowledgements

Firstly, I'd like to thank Dr. Chuck Harrell for this amazing opportunity to conduct my MS project and thesis in his lab. I first joined his lab for a rotation back in March 2022 after I had left a lab I had been in since September 2021. I didn't know how to do much besides a little bit of cell culture and scruffing a mouse, so I had much to learn. Already in the first week under his mentorship, I had learned a lot, such as how to analyze bulk RNAseq data and how to conduct immunohistochemical stains. Compared to my other rotations and previous lab experience at VCU, I was hooked and intrigued. I wanted to learn more about breast cancer and how to use all these analyses to come to a solution to better help patients suffering from this disease. Of course, I had a lot of maturation to go through as well before I could reach that point. I had to learn how to juggle my classes with lab work, how to handle difficult situations, and how to overcome hard times. My graduate studies here at VCU was not easy to say the least, and I struggled a lot. But despite all that, Chuck still supported me and helped me mature and grow into the scientist I am today. Without Chuck as my mentor, I wouldn't have been able to make it, and I likely would have given up. Chuck, thank you from the bottom of my heart for helping me find my North Star and for guiding me to become who I am meant to be. You've inspired me to continue with my PhD.

I want to thank my amazing lab mates (past and present) that have taught me valuable lessons on how to develop as a trainee and how to conduct science as a whole. David, thank you for helping me get settled in and for making everyday fun. Being around you has taught me how to not only think critically but also how to persevere even when lab work gets really tough and mentally fatiguing. Thank you, Emily, for being my buddy and always supporting me. I was able to learn a lot from you and I'll definitely use all your advice you've given me to make sure I can stay on the right path. Julia, thank you for always giving me something to look forward to and for being fun to hang around (and thanks for the treats you bring, they're yummy!). Also, thank you Carson for being reassuring and a bright light in the lab — I can't wait to see how your project progresses in the future. Thank you, Nicole, Rachel and Tess, for having done and doing the work you've done in the lab, such as cutting slides, doing tumor preps, treating and weighing some of my mice, and helping me with necropsies. Without you, it would have been much harder to get everything done that I needed to. Also, a huge thank you to Tia for laying the groundwork for this project, and for designing something so cool with huge promise. Hopefully this will benefit patients someday. Thank you to Narmeen, Alex, and Jayasree for helping me fit in with the lab and for helping me learn key methods. James, I hope you've enjoyed your summer studies in the lab, and I hope this experience helps you develop as a trainee. Nina, I hope that you enjoy your MD PhD in this lab, and I can't wait to see how your project develops and evolves.

I also want to thank my MS Thesis Committee, Dr. Tomasz Kordula, Dr. Erich Damm, and Dr. Jason Newton, for serving on my committee and for giving me insightful questions during and after my project proposal. I could not have gotten to where I am now without you. I would especially like to thank Dr. Tomasz Kordula and Dr. Maria Rivera for accepting me into VCU, for always having my back, and for never giving up on me. It really means a lot to me.

I'd also like to thank ASCB and the COMPASS committee (especially Scott, Sara, and Ankita) for helping me find joy in scientific outreach, and for helping me serve the scientific community in ways I never thought I could.

I want to also thank my amazing family. Dad, thank you for supporting me throughout my BS and MS studies, and for working hard all your life to give me a chance at having a good life, too. Mom, thank you for being there for me and for teaching me what it means to be strong and courageous. Megan, thank you for being my big sister and for always making me laugh. Ethan, thank you for being my little brother and for inspiring me to get physically fit. It fills me with joy to see all of you succeed, and hopefully we will get to where we are meant to be.

Thank you, Fatima, for being there for me and for supporting me through my BS and MS studies. You're a huge blessing in my life and I'm looking forward to the times we'll continue to have together in the future.

Finally, I would like to thank God for having blessed me with this opportunity to study in the US and finish my graduate studies here at VCU. The me two years ago would have never thought that I could mature and learn so much from being here. Through all the good and bad that I have experienced here, I thank you, Lord, for always being with me.

## Table of Contents

<b>List of Tables .....</b>	<b>V</b>
<b>List of Figures.....</b>	<b>VI</b>
<b>List of Supplementary Figures.....</b>	<b>VII</b>
<b>Abstract.....</b>	<b>1</b>
<b>Introduction.....</b>	<b>2</b>
<b>Materials &amp; Methods.....</b>	<b>11</b>
<b>Results .....</b>	<b>21</b>
<b>Discussion .....</b>	<b>33</b>
<b>References.....</b>	<b>36</b>
<b>Appendix.....</b>	<b>45</b>
<b>Vita .....</b>	<b>58</b>

## List of Tables

<b>Table 1: Basal-like TNBC PDX model information. ....</b>	<b>11</b>
<b>Table 2: 1° antibodies used for IHC experiments. ....</b>	<b>17</b>
<b>Table 3: 1° antibodies used for immunoblotting. ....</b>	<b>19</b>
<b>Supplementary Table 1: List of drugs of interest and genes encoding their drug target(s) compiled by Tia H. Turner. ....</b>	<b>45</b>
<b>Supplementary Table 2: p-values for PDX KPT-330 dose response data shown in Figure 1B calculated by Tia H. Turner. ....</b>	<b>46</b>
<b>Supplementary Table 3: Concentrations of drugs used in PDX dose response and synergism experiments shown in Figures 4-6 calculated by Tia H. Turner. ....</b>	<b>47</b>
<b>Supplementary Table 4: p-values for dose response data shown in Figure 4 calculated by Tia H. Turner. ....</b>	<b>48</b>

## List of Figures

Figure 1: <i>In vitro</i> efficacy of 34 blood-brain barrier permeable drugs and KPT-330 in basal-like TNBC PDXs identified by Tia H. Turner .....	4
Figure 2: Efficacy of 34 blood-brain barrier permeable drugs combined with KPT-330 in basal-like TNBC PDXs identified by Tia H. Turner .....	5
Figure 3: Dose responses of four basal-like TNBC PDXs to KPT-330 and five promising drug candidates conducted by Tia H. Turner .....	6
Figure 4: Drug combination analysis conducted by Tia H. Turner demonstrates synergism between KPT-330 and other blood-brain barrier permeable drugs in basal-like TNBC PDXs.....	7
Figure 5: Preliminary <i>in vivo</i> assessment of average WHIM2 MGT burden over time after treatment with therapy .....	8
Figure 6: Selected compounds of interest for the treatment of TNBC and brain metastatic disease .....	9
Figure 7: Bulk RNA-seq expression analysis of KPT-330 and everolimus protein targets and downstream affected proteins .....	21
Figure 8: Single-cell RNA-seq expression analysis of KPT-330 and everolimus protein targets and downstream affected proteins .....	22
Figure 9: Validation of XPO1 expression in WHIM2 and HCI-001 PDX tissue and increased FKBP1A expression in WHIM2 compared to HCI-001 .....	23
Figure 10: <i>In vivo</i> assessment of average WHIM2 MGT burden over time after treatment with therapy .....	24
Figure 11: <i>In vivo</i> assessment of average HCI-001 MGT burden over time after treatment with therapy .....	25
Figure 12: <i>In vivo</i> assessment of average WHIM2 total metastasis burden at day 35 since seeding after four weeks of treatment with therapy .....	27
Figure 13: <i>Ex vivo</i> assessment of average WHIM2 brain metastasis burden at day 35 since seeding after four weeks of treatment with therapy .....	28
Figure 14: <i>Ex vivo</i> assessment of average WHIM2 ovary metastasis burden at day 35 since seeding after four weeks of treatment with therapy .....	29
Figure 15: <i>Ex vivo</i> assessment of average WHIM2 liver metastasis burden at day 35 since seeding after four weeks of treatment with therapy .....	30
Figure 16: <i>Ex vivo</i> assessment of average WHIM2 lung metastasis burden at day 35 since seeding after four weeks of treatment with therapy .....	31
Figure 17: Immunoblot of mechanism of action of KPT-330 + everolimus in WHIM2 TNBC PDXs.....	32

## List of Supplementary Figures

Supplementary Figure 1: <i>In vitro</i> efficacy of 34 drugs alone and combined with KPT-330 in HCI-001 PDX cells assessed by Tia H. Turner .....	49
Supplementary Figure 2: <i>In vitro</i> efficacy of 34 drugs alone and combined with KPT-330 in UCD52 PDX cells assessed by Tia H. Turner .....	50
Supplementary Figure 3: <i>In vitro</i> efficacy of 34 drugs alone and combined with KPT-330 in WHIM2 PDX cells assessed by Tia H. Turner .....	51
Supplementary Figure 4: <i>In vitro</i> efficacy of 34 drugs alone and combined with KPT-330 in WHIM30 PDX cells assessed by Tia H. Turner .....	52
Supplementary Figure 5: Dose-response curves for five drugs of interest in basal-like TNBC PDXs conducted by Tia H. Turner .....	53
Supplementary Figure 6: Preliminary <i>in vivo</i> study average mouse weights .....	54
Supplementary Figure 7: WHIM2 <i>in vivo</i> study average mouse weights .....	55
Supplementary Figure 8: HCI-001 <i>in vivo</i> study average mouse weights.....	56
Supplementary Figure 9: Metastasis <i>in vivo</i> study average mouse weights.....	57
Supplementary Figure 10: Total metastasis spread over time.....	57



## Abstract

### **KPT-330 synergizes with everolimus to reduce mTORC1-overactive basal-like triple-negative breast cancer brain metastasis burden**

By Aaron D. Valentine

A thesis submitted in partial fulfillment of the requirements for the degree of Master of Science at Virginia Commonwealth University.

Virginia Commonwealth University 2023

Major Director: J. Chuck Harrell, PhD, Associate Professor, Department of Pathology

Triple-negative breast cancer (TNBC), a highly metastatic breast cancer subtype, accounts for approximately 20% of all breast cancer diagnoses. Basal-like TNBC is notably difficult to treat due to the lack of actionable drug targets such as estrogen and progesterone receptors, as well as HER2. Due to the deficiency in TNBC-targeting drugs that are able to cross the blood-brain barrier (BBB) for breast-to-brain metastasis, there is a need to develop novel BBB-permeable treatments. After preliminary testing, KPT-330 (XPO1 inhibitor) and everolimus (FKBP1A/mTOR inhibitor) were selected as drug candidates for this study. Patient-derived xenograft (PDX) models for in vitro and in vivo studies were chosen based on the relative transcriptomic and proteomic expression of XPO1 and FKBP1A. KPT-330, everolimus, and KPT-330 + everolimus were assessed in NSG mice with mammary gland tumors or metastases. KPT-330 + everolimus significantly reduced an mTORC1-overactive PDX primary tumor burden compared to single agents and vehicle control, whereas an mTORC1-underactive PDX primary tumor burden was not significantly reduced upon treatment. Further testing of the affected PDX determined that the metastasis burden in the brain and ovaries was significantly reduced upon treatment with KPT-330 + everolimus. Therefore, the proposed treatment may be effective in improving the outcome of patients suffering from mTORC1-overactive TNBC surgically non-resectable metastases. FKBP1A expression could serve as a biomarker for future treatment selection for TNBC.

*Keywords: breast cancer, triple-negative, metastasis, preclinical, pharmacogenomics*

## Introduction

### *Triple-negative breast cancer statistics and diagnostics*

According to the American Cancer Society, an estimated 297,790 women will be diagnosed with breast cancer and 43,700 will die due to advanced disease that does not respond to current standard-of-care. Furthermore, approximately 1 in 39 women will die from breast cancer – this being the second most deadly disease for women. Breast cancer can be divided into four intrinsic subtypes: Luminal A (estrogen receptor (ER) and progesterone receptor (PR) positive), Luminal B (ER+ and PR-), basal-like breast cancer, and human epidermal growth factor receptor 2 (HER2) enriched breast cancer [1]. On the other hand, breast cancer can also be defined by which receptors it expresses: Hormone positive (HR+) breast cancer, which includes ER+ and PR+ breast cancer, HER2 enriched breast cancer, and triple-negative breast cancer (TNBC) [2, 3]. TNBC is a highly metastatic subtype and accounts for 20% of all diagnoses [4]. The lack of ER, PR, and HER2 makes this subtype especially difficult to target and treat with chemotherapy in the clinic. As such, TNBC has the worst prognosis compared to all other breast cancer subtypes [5]. Intrinsic subtyping and subtyping based on the presence of key receptors are directly linked – basal-like tumors account for roughly 80% of all TNBCs, with the other 20% being classified as non-basal-like TNBCs [6].

TNBC can be classified into further subtypes based on the expression of other proteins. Claudin-low TNBC, for example, is defined by a low gene expression of the tight junction proteins claudin 3, 4, and 7 and the calcium-dependent cell-cell adhesion glycoprotein e-cadherin, thus lacking epithelial cell features which would otherwise be common [7]. A TNBC subtyping strategy known as Lehmann subtyping identified six different TNBC subtypes through cluster analysis: the basal-like 1 and 2 (BL1, BL2) subtypes, which have higher cell cycle and DNA damage response gene expression, the immunomodulatory (IM) subtype, which has increased immune cell signaling and signal transduction, the mesenchymal (M) and mesenchymal stem-like (MSL) subtypes, which are both enriched for epithelial-mesenchymal transition (EMT), and the luminal androgen receptor (LAR) subtype, which is characterized by androgen receptor (AR) signaling [8].

TNBC treatments are often limited to neoadjuvant chemotherapy, surgery, and radiation. Chemotherapy is highly toxic to patients and often ineffective in treating advanced disease due to intrinsic or acquired chemoresistance [9-11]. TNBC has the greatest risk of metastasis and progression-free survival is significantly reduced [9].

### *Metastatic potential of triple-negative breast cancer*

Metastasis involves the development and spread of secondary distant or nearby tumoral masses from a primary tumor [12]. This hallmark of cancer is streamlined by cancer cell detachment followed by migration and circulation of cancer cells through the bloodstream, extravasation, and the formation of metastatic tumor microenvironments and niches in distant tissues [13]. For a primary tumor to form metastatic niches in other tissues, a process known as epithelial-mesenchymal transition (EMT) usually occurs. This mechanism necessitates the loss of epithelial markers such as e-cadherin and various cytokeratins and the gain of mesenchymal markers such as vimentin and fibronectin [14]. Typically, this procedure is promoted through the acquisition of

mutations – one example involving amplified interleukin-6 expression, which suppresses e-cadherin expression and promotes vimentin upregulation [14].

TNBC is highly invasive with a distant metastasis rate of 46% in patients [15]. Preferentially, TNBC metastasizes to the brain, liver, and lungs [16, 17]. Although rare, metastasis to the ovaries may also occur [18, 19]. Of the histologic subtypes of breast cancer, TNBC has the highest risk of brain metastasis, and TNBC brain metastases are notably aggressive [20-23]. Recent studies have shown that due to the aggressiveness of metastatic TNBC (mTNBC), patients have a higher incidence of early brain metastasis occurrence [24], which is worsened by the median survival rate being as short as five months [25]. This is majorly due to the limitations of current pharmaceuticals able to reach the brain metastases, notably because of the blood-brain barrier (BBB), which generally only allows lipophilic and low molecular weight compounds to enter the brain [26]. The cellular structure of the BBB itself impacts the BBB-permeability of therapeutic compounds. The most important cellular components which restrict permeability or reduce the free movement of solutes and other cellular elements, are endothelial cells, pericytes and astrocytes. In particular, the movement of compounds is restricted by the tight junctions between the basal membrane of the BBB and the endothelial cells of the vasculature, with the astrocyte end feet forming the BBB at the basal membrane [27]. Given that a majority of chemotherapeutics are unable to cross the BBB, it is critical to develop new treatments that are both more efficacious and BBB-permeable.

#### *Utilization of KPT-330 in combination with BBB-permeable therapeutics*

Based on previous drug screening data in patient-derived xenograft (PDX) models of TNBC [28], 34 BBB penetrating drugs with significant *in vitro* cytotoxicity were identified (Figure 1A). Alongside these findings, we were interested in the compound Selinexor (KPT-330) (Figure 1B), a selective inhibitor of nuclear export (SINE). This FDA-approved compound is able to cross the BBB and has historically shown significant effectiveness in the primary tumor setting *in vivo* [29] and inhibits Exportin-1 (XPO1) [30, 31], a subclass of karyopherin [32]. Specifically, KPT-330 and other SINEs were developed utilizing Structure-Activity Relationship (SAR) technology and computational modeling with consensus induced fit docking (cIFD) in mind [33]. This allows for these compounds to covalently bind the cargo-binding pocket of XPO1, thus inhibiting cargo-XPO1 interaction [34, 35]. XPO1 facilitates the transport of both RNA and proteins larger than 65 kDa, and this process is mediated by Ran GTPase [36]. Inhibiting XPO1 prevents the nuclear export of over 200 proteins, including some tumor suppressors such as Survivin, p53, BRCA1, BRCA2, and Cyclin D1 [37, 38]. Inhibition of the nuclear export of these tumor suppressors leads ultimately to apoptosis and cell death [39, 40].

Although KPT-330 has demonstrated *in vivo* efficacy in a mouse model of TNBC brain metastasis [41], a phase II clinical trial of KPT-330 in mTNBC demonstrated a 30% clinical benefit rate which did not meet the efficacy threshold [37]. Despite this outcome, XPO1 expression is negatively associated with brain metastasis-free survival [29], which suggests that KPT-330 may have a benefit in patients with basal-like TNBC brain metastases if paired with suitable therapeutic agents.

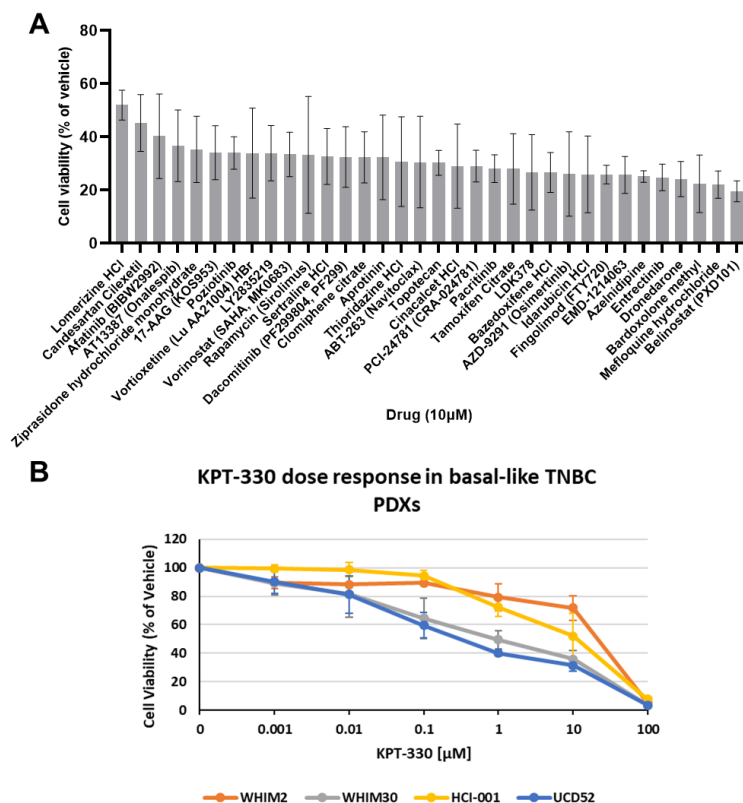


**Figure 1: *In vitro* efficacy of 34 blood-brain barrier permeable drugs and KPT-330 in basal-like TNBC PDXs identified by Tia H. Turner.** (A) Average cell viability across 4 PDXs: HCI-001 (n = 3), UCD52 (n = 3), WHIM2 (n = 5), WHIM30 (n = 3) in response to 34 drugs at 10 μM; n represents a number of independent experiments, each performed in duplicate; error bars represent standard deviation of averaged data. Data were obtained from high-throughput drug screening. 34 drugs selected are listed along with their targets in Supplementary Table 1. (B) Cell viability (percent of vehicle) in response to increasing concentrations of KPT-330 for each of the 4 indicated PDXs; three independent experiments, each in triplicate, were performed per PDX. Error bars represent the standard deviation between independent experiments; p-values are listed in Supplementary Table 2.

To identify potentially synergistic drugs with KPT-330, a preliminary combination screening was performed by Tia H. Turner, a previous student in the lab. This tested each of the 34 drugs alone and with KPT-330 in four basal-like TNBC PDXs: WHIM2, WHIM30, HCI-001, and UCD52 (Figure 2). Depending on the cell viability of these combination screens, a difference in percent inhibition was calculated which allowed for the assessment of supra-additive (> 0), additive (= 0), or sub-additive (< 0) trends.

Mefloquine exhibited strong supra-additive trends in combination with KPT-330 in HCI-001 (Figure 2; Supplementary Figure 1B-C), UCD52 (Figure 2; Supplementary Figure 2B-C), and WHIM30 (Figure 2; Supplementary Figure 4B-C), but not in WHIM2 (Figure 2; Supplementary Figure 3B-C). Azelnidipine exhibited supra-additive trends in combination with KPT-330 in HCI-001 (Figure 2; Supplementary Figure 1B-C) and UCD52 (Figure 2; Supplementary Figure 2B-C), weak supra-additive trends in WHIM2 (Figure 2; Supplementary Figure 3B-C), and weak sub-additive trends in WHIM30 (Figure 2; Supplementary Figure 4B-C). Most of the other drugs showed variable additive or sub-additive trends across the PDXs. Several drugs, including Bardoxolone-methyl, 17-AAG, Navitoclax, Belinostat, and Entrectinib, appeared to have sub-

additive trends when combined with KPT-330 in most or all of the PDXs (Figure 2), however, this could be explained by their relatively strong cytotoxicity as single agents at the doses tested in several of the PDXs (Supplementary Figures 1B-4B & 1C-4C). It should be noted that KPT-330 did not exhibit the necessary levels of cytotoxicity in UCD52 and WHIM2 at the doses used in these studies (Supplementary Figures 2B-C and 4B-C), which may account for inaccurate estimates of combinatorial effects. Despite the limitations of this study, our findings revealed several drug candidates for further studies.

Given these collective findings, Tanespimycin (17-AAG; HSP90 inhibitor), Azelnidipine (dihydropyridine calcium channel blocker), Belinostat (pan-HDAC inhibitor), Entrectinib (selective tyrosine kinase inhibitor), and Mefloquine (anti-malarial) were selected for synergism testing in combination with KPT-330. Dose-response experiments demonstrated dose-dependent cytotoxicity of all five drugs in the four PDXs (Supplementary Figure 5).

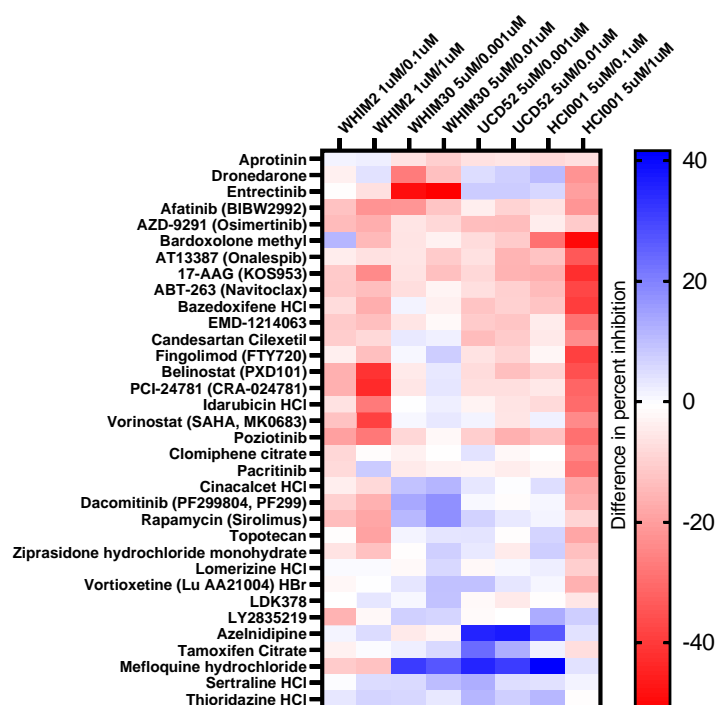


**Figure 2: Efficacy of 34 blood-brain barrier permeable drugs combined with KPT-330 in basal-like TNBC PDXs identified by Tia H. Turner.** PDX cells (HCI-001, UCD52, WHIM2, WHIM30) were treated with the 34 indicated drugs at a single dose alone or in combination with KPT-330 at two different doses. The difference in percent inhibition of cell viability was calculated for each drug combination: (percent inhibition of combination) – [(percent inhibition of drug 1 alone) + (percent inhibition of drug 2 alone)]. The heatmap depicts the relative difference in percent inhibition across the 4 PDXs; one independent experiment was performed in triplicate per dose combination per PDX. Dose combinations are indicated next to PDX labels (corresponding drug/KPT-330). Graphs depicting corresponding cell viability data for these experiments are shown in Supplementary Figures 1-4.

Preliminarily, to identify which of the five selected drugs have synergistic effects when combined with KPT-330 *in vitro*, Tia H. Turner treated PDXs (HCI-001, UCD52, WHIM2, WHIM30) with 7 concentrations of each drug alone, seven concentrations of KPT-330 alone, and combinations of each drug and KPT-330 at the corresponding doses to maintain a constant dose ratio. Drug concentrations were determined based on previous dose-response experiments (Figure 1B;

Supplementary Figure 5) and tailored to each PDX (Supplementary Table 3) to achieve consistent dose-response curves for subsequent analyses. Each of the drugs had significant dose-dependent cytotoxicity in the four PDXs (Figure 3; Supplementary Table 4).

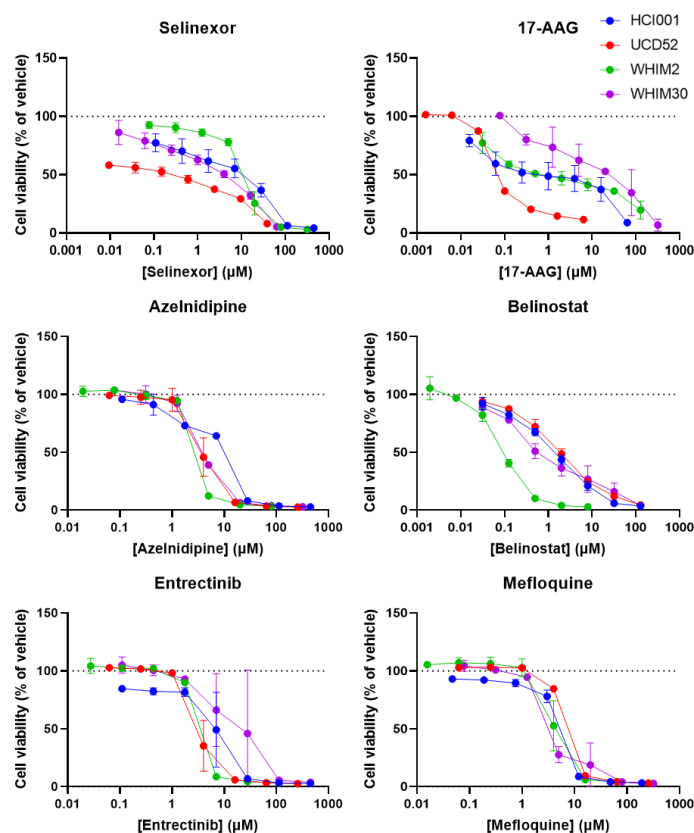


**Figure 3: Dose responses of four basal-like TNBC PDXs to KPT-330 and five promising drug candidates conducted by Tia H. Turner.** Graphs depict cell viability (percent of vehicle) in response to increasing concentrations of the indicated drugs in 4 PDXs (HCI-001, UCD52, WHIM2, WHIM30); these are the single-agent data used for subsequent synergism experiments. Drug concentrations were tailored to each PDX and are listed in Supplementary Table 3. Two independent experiments were performed in triplicate per PDX; error bars represent the standard deviation between independent experiments; p-values are listed in Supplementary Table 4.

To assess synergism among the five drug combinations, cell viability data were converted to fraction inhibition (Fa) values and analyzed using CompuSyn [42, 43]. Combinations were considered synergistic if the combination index (CI) was less than 1 at Fa values greater than 0.75. KPT-330 was found to be synergistic with 17-AAG in HCI-001 and WHIM2; with Azelnidipine, Belinostat, and Mefloquine in HCI-001, UCD52, and WHIM30; and with Entrectinib in all four PDXs, except for two data points at the highest Fa values which did not have synergistic CI values in WHIM2 (Figure 4).

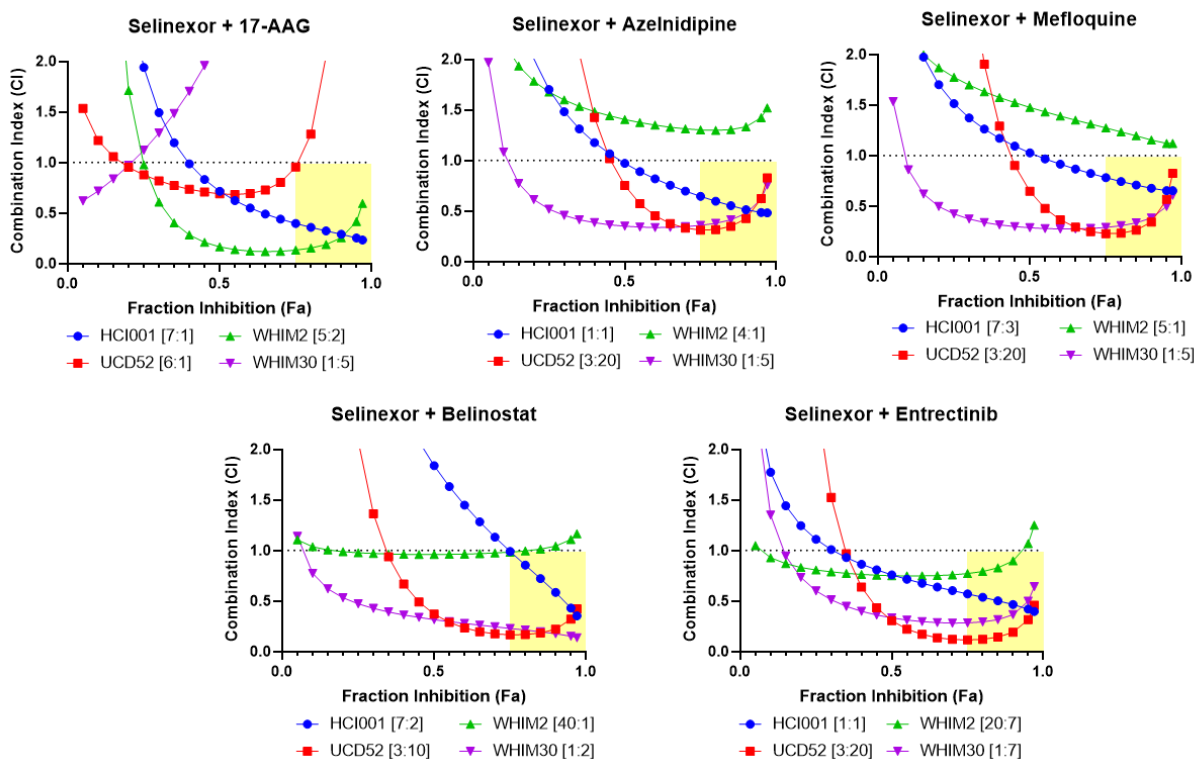


**Figure 4: Drug combination analysis conducted by Tia H. Turner demonstrated synergism between KPT-330 and other blood-brain barrier permeable drugs in basal-like TNBC PDXs.** PDX cells (HCI-001, UCD52, WHIM2, WHIM30) were treated with KPT-330 and each indicated drug both alone and in combination at constant dose ratios (indicated in graph legends for each drug combination and PDX). Cell viability data were converted to fraction inhibition (Fa), and combination index (CI) values were calculated using CompuSyn software; graphs depict Fa-CI plots to assess for synergism (CI < 1), additivity (CI = 1), or antagonism (CI > 1). Yellow highlighted regions represent synergism (CI < 1) at optimal efficacy levels (Fa > 0.75).

After determining that these drugs were synergistic with KPT-330 *in vitro*, the next step was to test them with KPT-330 *in vivo* in mammary gland tumors (MGT). Due to Bristol-Myers Squibb halting production of 17-AAG, albeit for reasons unrelated to its clinical potential, this compound was no longer pursued in this study [44]. This left only Azelnidipine, Entrectinib, Belinostat, and Mefloquine to be tested with KPT-330. These agents were selected for further study in WHIM2 (Figure 5).

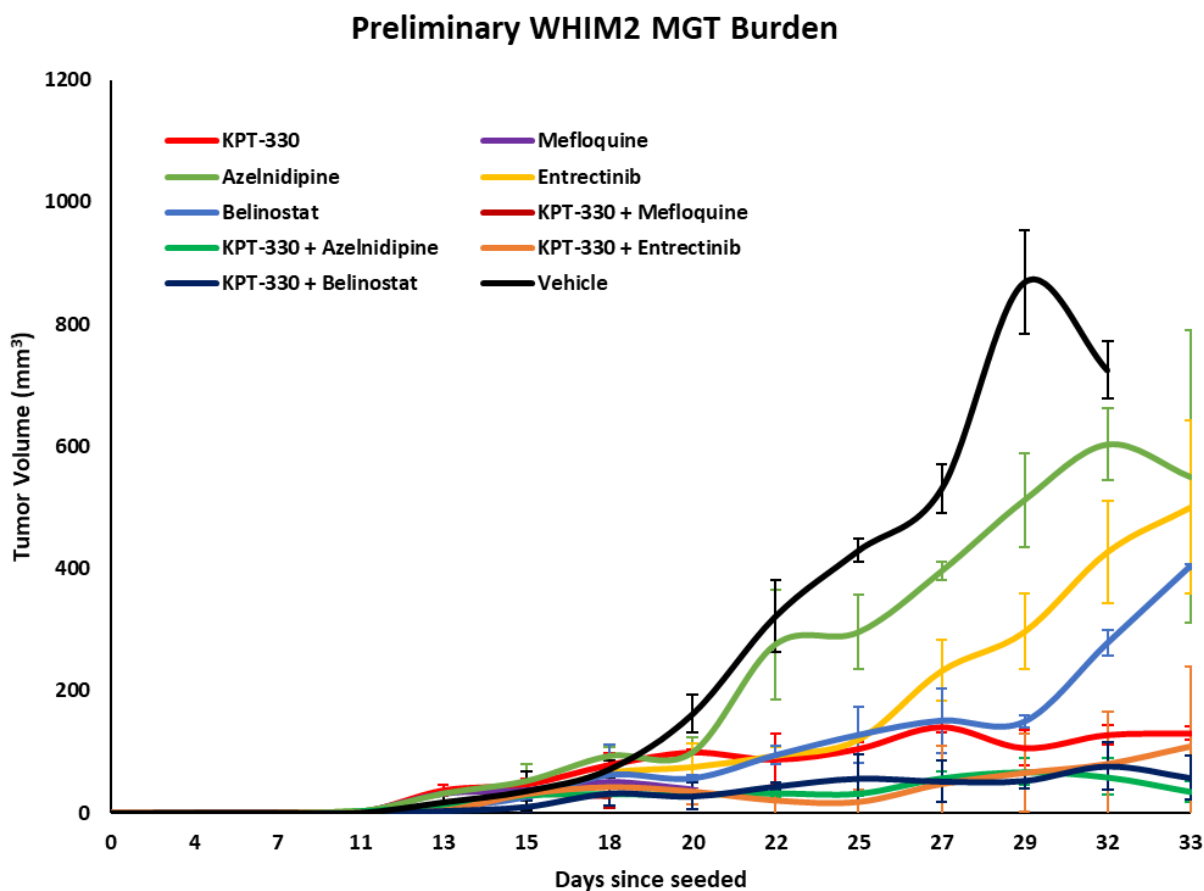


**Figure 5: Preliminary *in vivo* assessment of average WHIM2 MGT burden over time after treatment with therapy.** *In vivo* tumor burden after treatment with vehicle (black), KPT-330 (red), Mefloquine (purple), Azelnidipine (light green), Entrectinib (yellow), Belinostat (blue), KPT-330 + Mefloquine (brown), KPT-330 + Azelnidipine (dark green), KPT-330 + Entrectinib (orange) and KPT-330 + Belinostat (indigo), with  $n = 2$  per group. Tumor burden is measured as tumor volume (y-axis,  $\text{mm}^3$ ) by days since seeded (x-axis). Treatments started on day 13 since seeded (red arrow). One-way ANOVA was performed to assess differences in tumor volume between KPT-330 + Azelnidipine, Entrectinib, or Belinostat treatment groups and the single-agent treatment groups, where  $p < 0.05$  was considered statistically significant. To assess the toxicity of the compounds, the mice were weighed over time (Supplementary Figure 6).

All WHIM2 tumors treated with KPT-330 and its respective combinations with Azelnidipine, Entrectinib, and Belinostat decreased in tumor volume compared to the vehicle-treated group (Figure 5). The Azelnidipine, Entrectinib, Belinostat, and Mefloquine single agents had no significant effect on tumor volume (Figure 5). Mefloquine and its respective combination treatment with KPT-330 were associated with significant weight loss and death of the mice, while all other single-agents and combination treatments appeared to be non-toxic and had no significant repercussions on mouse body weight (Supplementary Figure 6). However, there was no significant difference in tumor volume between the KPT-330-treated group and respective combination therapy groups with Azelnidipine, Entrectinib, and Belinostat, suggesting that KPT-330 drives the phenotype of treatment in these WHIM2-burdened mice when paired with either of these three drugs.



## Targeting of XPO1 and FKBP1A

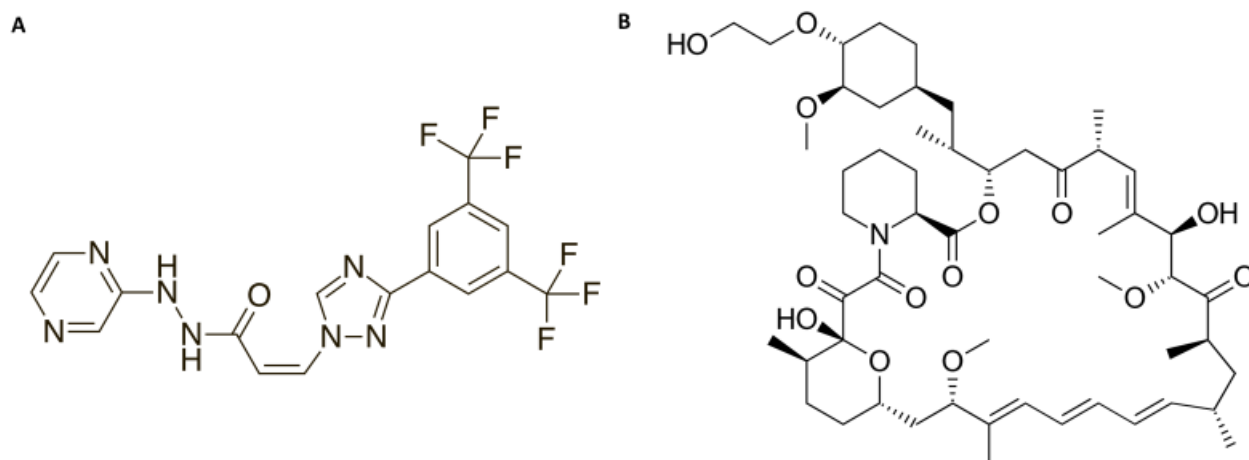


**Figure 6: Selected compounds of interest for the treatment of TNBC and brain metastatic disease.** (A) Chemical structure of KPT-330. (B) Chemical structure of everolimus.

After conducting an initial test using KPT-330 (Figure 6A) in combination with Azelnidipine, Entrectinib, Mefloquine, and Belinostat, we observed that there were no significant effects on tumor burden compared to using KPT-330 alone (Figure 5). Consequently, we decided to reassess our analysis to identify suitable drugs that can be combined with KPT-330 and penetrate the BBB. We discovered that Rapamycin, an antifungal and mTOR inhibitor, demonstrated promising responses in our *in vitro* experiments (Figure 1; Figure 2). However, due to Rapamycin having limitations in its pharmacokinetic properties [45], we chose to explore its second-generation derivative known as everolimus (Figure 6B). This is a classical mTORC1 inhibitor and FDA-approved BBB-permeable compound for the treatment of subependymal giant cell astrocytoma (SEGA) [46]. This drug is also approved for use in renal cell carcinoma due to its action on the PI3K pathway via mTORC1 inhibition [45]. Everolimus acts by binding irreversibly to FK506 Binding Protein Prolyl Isomerase 1A (FKBP1A) [47, 48], which induces a conformational change in the protein structure of FKBP1A. This leads to the inhibition of mTORC1 and resulting from this is the inability of the tumor to proliferate and reproduce due to the upregulation of apoptotic proteins, thus leading to a reduction of cell proliferation, angiogenesis, and tumor cell death [47, 48]. While everolimus is mostly known for its action on FKBP1A, it has also been shown to inhibit HIF-1 $\alpha$  and other associated pathways such as STAT3 and VEGF in TP53 head and neck squamous cell carcinoma (HNSCC) patients [49], including the subtype oral squamous cell carcinoma (OSCC) [50].

### Research approach and hypothesis

We hypothesized that FKBP1A expression can serve as a biomarker to target mTORC1-overactive TNBC primary tumor and brain metastases by utilizing KPT-330 in combination with everolimus. To test this hypothesis, the following objectives were addressed: (1) To determine if KPT-330 and everolimus individually or when combined are effective at reducing mammary tumor growth *in vivo*; (2) To determine if these drugs are effective at inhibiting metastatic growth in different

organs, including the brain; (3) To validate the mechanism of action of KPT-330 and everolimus in TNBC PDXs.

While the mechanism of action for KPT-330 and everolimus is already known for other models, they had to be confirmed in our TNBC PDX models. Mechanistically, an increase of unbound cargo proteins in the nucleus, with a reduction of these compounds in the cytoplasm would indicate KPT-330 activity [51, 52]. A reduction of phospho-rpS6 in the nucleus and cytoplasm would serve as an indication of mechanistic action of everolimus due to the inhibition of mTORC1 and PI3K signaling pathways, allowing for cap-independent translation, thus inducing apoptosis [48, 53, 54].

Because of the poor prognosis of basal-like TNBC, there is a need for more effective treatment to improve survivability. Furthermore, breast-to-brain metastasis has one of the poorest prognoses compared to other breast-to-organ metastases. In addition to the difficulty of treating TNBC due to the absence of ER, PR and HER2, the lack of available therapeutic compounds able to cross the BBB is a hinderance. If the evaluation of KPT-330 + everolimus is effective in MGTs and brain metastases, this could open a new avenue for patient survival and increased life expectancy.

## Materials & Methods

### *Mice*

NOD *scid* gamma (NSG) were used for this study due to their lack of functional T-cells and B-cells and a normal hematopoietic microenvironment [55]. This allows for this animal model to harbor and cultivate human PDX tissue. All NSG mice were obtained from and generated by the Virginia Commonwealth University Cancer Mouse Models Core Laboratory, supported, in part, with funding to the Massey Cancer Center from NIH-NCI Cancer Center Support Grant P30 CA016059. All studies involving the use of mice were approved by the VCU IACUC, and all experiments were performed according to IACUC guidelines.

### *TNBC PDX models*

Two models were utilized for this study: WHIM2 (Washington Human in Mouse 2, Washington University St. Louis, St. Louis MO, USA) and HCI-001 (Huntsman Cancer Institute 001, Huntsman Cancer Institute, Salt Lake City UT, USA). For the *in vitro* analyses, four basal-like TNBC PDX models were used for the experiments performed in this study: HCI-001, WHIM2, WHIM30 (Washington Human in Mouse 30, Washington University St. Louis, St. Louis MO, USA), and UCD52 (University of Colorado 52, University of Colorado Denver, Denver CO, USA) (Table 1).

**Table 1: Basal-like TNBC PDX model information [56, 57].**

PDX Model	Gender	Race	Vital Status	Diagnosis Age	Intrinsic Subtype	Metastasis Sites
HCI-001	Female	Caucasian	Deceased	39.5	Triple Negative, Basal-like	Lung
WHIM2	Female	African American	Deceased	44	Triple Negative, Basal-like	Brain
WHIM30	Female	Asian	Alive at reporting	35	Triple Negative, Basal-like	None
UCD52	Female	Caucasian	Unknown	Unknown	Triple Negative, Basal-like	Unknown

### *Cell viability assays*

For all *in vitro* drug response experiments, PDX cells were plated in 96-well plates at 25,000 cells per well in M87 medium and treated with drugs for 72 hours. Cell viability was measured using the CellTiter-Glo Luminescent Viability Assay (Promega). Data were converted to percent of vehicle (DMSO) viability for analyses.

### *High-throughput drug screening*

High-throughput screening of 514 drugs (ApexBT), selected based on our previous PDX drug screens [28, 29], was performed in four basal-like TNBC PDXs (HCI-001, UCD52, WHIM2, WHIM30). PDX cells were plated and treated with drugs at 10  $\mu$ M using an Integra Assist Plus Pipetting Robot with VIAFLO and VOYAGER electronic multichannel pipettes (Integra), and cell viability was measured as described above. For analyses, cell viability data from independent experiments, each performed in duplicate, were averaged for each PDX.

### *Selection of drugs for in vitro studies*

The 514-drug screening data were used to select drugs of interest for testing in combination with selinexor in subsequent experiments. We initially identified 86 drugs that were greater than 40% cytotoxic (cell viability < 60% of vehicle) across four basal-like TNBC PDXs (HCI-001, UCD52, WHIM2, WHIM30). This list was then narrowed down to the following 34 drugs based on ability to cross the BBB: Lomerizine, Candesartan, Afatinib, Onalespib, Ziprasidone, 17-AAG, Pozotinib, Vortioxetine, LY2835219, Vorinostat, Rapamycin, Sertraline, Dacomitinib, Clomiphene, Aprotinin, Thioridazine, Navitoclax, Topotecan, Cinacalcet, PCI-24781, Pacritinib, Tamoxifen, LDK378, Bazedoxifene, AZD-9291, Idarubicin, Fingolimod, EMD-1214063, Azelnidipine, Entrectinib, Dronedarone, Bardoxolone-methyl, Mefloquine, and Belinostat (Supplementary Table 1). All drugs, including KPT-330, were purchased from ApexBT for use in *in vitro* experiments.

### *In vitro single-agent dose-response studies*

To determine optimal dosing for subsequent *in vitro* drug combination experiments, PDX cells (HCI-001, UCD52, WHIM2, WHIM30) were treated for 72 hours with increasing doses of KPT-330 (ranging from 0.001 to 100  $\mu$ M) in triplicate, as well as two doses (1 and 10  $\mu$ M) of each of the 34 drugs identified above in quadruplicate. Cell viability was measured as described above.

### *In vitro drug combination screening studies*

To help identify drugs of interest for subsequent synergism studies in combination with KPT-330, PDX cells (HCI-001, UCD52, WHIM2, WHIM30) were treated for 72 hours with each of the 34 drugs listed above at one dose per PDX (1  $\mu$ M for WHIM2; 5  $\mu$ M for HCI-001, UCD52, and WHIM30), alone and in combination with KPT-330 at two different doses per PDX (0.1 and 1  $\mu$ M for HCI-001 and WHIM2; 0.001 and 0.01  $\mu$ M for UCD52 and WHIM30). These doses were determined based on prior single-agent studies. Cell viability was measured as described above. To assess combinatorial effects, the difference in percent inhibition between each drug as a single agent and in combination was calculated from percent cell viability values as described previously [28]. Drug combinations with a positive difference in percent inhibition were considered to have supra-additive trends, and those with a negative difference in percent inhibition were considered to have sub-additive trends.

### *In vitro synergism studies*

Based on efficacy and/or supra-additive trends in the studies described above, along with gene expression analyses, five drugs were selected for synergism testing in combination with KPT-330: 17-AAG, Azelnidipine, Belinostat, Entrectinib, and Mefloquine. To determine optimal dosing for synergism studies, PDX cells (HCI-001, UCD52, WHIM2, WHIM30) were treated with increasing concentrations of each drug (ranging from 0.001 to 100  $\mu$ M) in triplicate. The data obtained from these initial dose-response experiments, as well as the prior KPT-330 dose-response experiments, were used to tailor the concentrations of each drug to each PDX line. For synergism experiments, PDX cells (HCI-001, UCD52, WHIM2, WHIM30) were treated for 72 hours with seven doses of selinexor alone, seven doses of each of the five drugs alone, and KPT-330 combined with each of the five drugs at the corresponding doses, maintaining a constant dose ratio. Two independent experiments, each in triplicate, were performed for each PDX line. Cell viability was measured as described above, and data (average percent of vehicle of triplicates) were converted to fraction inhibition (Fa). Combination index (CI) and dose reduction index (DRI) were calculated for each drug combination using CompuSyn software, which employs the Chou-Talalay method of drug combination analysis [42, 43]. CI and DRI values for each independent experiment were averaged and used to generate Fa-CI and Fa-DRI plots.

### *Bulk RNA-seq*

Dry ice flash-frozen tumors were processed using Qiagen Rneasy Kit in conjunction with QIAshredder tubes and RNA Zap. The quality of the sample was tested using Nanodrop. To construct the library, the RNA sample was first quantified with the Qubit 2.0 Fluorometer (ThermoFisher Scientific, Waltham, MA, USA) and checked for its integrity with TapeStation (Agilent Technologies, Santa Clara, CA, USA). Then, NEBNext Ultra II RNA Library Prep Kit for Illumina was used to prepare the RNA sequencing library according to manufacturer's instructions (New England Biolabs, Ipswich, MA, USA). Afterward, the mRNAs were briefly enriched with Oligod(T) beads and then fragmented for 15 minutes at 94 °C. Subsequently, the first- and second-strand cDNA fragments were synthesized, after which their 3' ends were end-repaired and adenylated. Following this, universal adapters were ligated to the cDNA fragments, and then index addition and library enrichment via PCR were performed with limited cycles. Finally, to validate the finished sequencing library, Agilent TapeStation (Agilent Technologies) was used, and the library was quantified with the Qubit 2.0 Fluorometer (ThermoFisher Scientific) as well as by quantitative PCR (KAPA Biosystems, Wilmington, MA, USA).

Sequencing was performed by Azenta. Sequencing libraries were first multiplexed and clustered onto a flow cell, after which the flow cell was inserted into the Illumina HiSeq 4000 instrument according to the manufacturer's instructions. A 2 × 150 bp paired-end (PE) configuration was selected to sequence the samples. The HiSeq Control Software (HCS) was utilized to conduct image analysis and base calling. Once the raw BCL data were generated, it was converted into FASTQ format and demultiplexed with the Illumina BCL2FASTQ 2.17 program. For index sequence identification, one mismatch was allowed. Bulk RNA-seq data was analyzed and formatted into a heatmap using Morpheus (<https://software.broadinstitute.org/morpheus/>).

### *Bulk RNA-seq quality control & preprocessing*

Bulk RNA-seq data were preprocessed as previously described [58]. FastQC v0.11.8 [59] was used to assess sequencing quality and adapters and low-quality base pairs were removed using CutAdapt v1.15 [60]. High-quality reads were aligned to a merged human/mouse genome using STAR v2.5.2b [61] with the following command line options: “--outSAMtype BAM Unsorted --outSAMorder Paired --outReadsUnmapped Fastx --quantMode TranscriptomeSAM --outFilterMultimapNmax 1. The Salmon v0.8.2” [62] “quant” algorithm was used to obtain read counts from the aligned BAM files using the “IU” library type. Read counts were loaded into R to calculate Log<sub>2</sub> TPM (transcript per million) values used for gene signature computations (methods below) and PAM50 subtyping using the genefu v2.11.2 R package [63].

### *Single-cell RNA-seq, quality control & preprocessing*

Single-cell RNA-Seq (scRNA-Seq) was performed on four TNBC cell lines (HCC1143, HCC1187, MDA-MB-468, and SUM149) and 13 PDX samples using the Chromium single Cell Gene Expression Kit (10x Genomics) per the manufacturer’s protocol and sequenced in the VCU Genomics core. The TNBC cell line samples were aligned to the GRCh38 version of the human genome and gene expression was calculated using the 10x Genomics CellRanger v6.0 software suite of tools. Dead and poor-quality cell removal was performed using an in-house R v4.1.3 script with the Seurat v4.3.0 package [64]. Briefly, cutoffs for the number of genes detected (nFeature), number of molecules detected (nCount), and percent mitochondrial expression (percent.mt) were calculated for each sample individually using 3 median absolute deviations (MADs) above the median value for that sample (the median for the percent.mt attribute was calculated using only cells with  $\leq 50\%$  mitochondrial expression). Cells were deemed poor quality if their nFeature or nCount value was greater than 3 MADs from the median in either direction, and if the percent.mt was above the 3 MAD cutoff, or a hard cutoff of 25%, whichever was lower. PDX samples followed a similar pipeline, however, they were first aligned to the 10x Genomics merged human/mouse genome (human genome version GRCh38 and mouse genome version mm10) to identify and remove mouse cells. Once mouse cells were removed the remaining human cells were re-aligned to the GRCh38 human genome, followed by the dead and poor-quality cell filtering described above. All PDX samples were then normalized using log normalization and merged using Seurat’s *merge()* function. A principal component analysis (PCA) was performed using a 100-gene PI3K activity signature from [65], instead of the default most variable features in the Seurat pipeline. This modified PCA matrix was utilized for the generation of UMAP and t-SNE visualizations, as well as Seurat’s graph-based clustering. An in-house script was then used to export the Seurat object to a 10x Genomics formatted file, and the CellRanger “reanalyze” function was run to reformat the data so that it could be imported into the 10x Loupe Cell Browser v6.

### *In vivo PDX primary mammary gland tumor burden studies*

For the preliminary *in vivo* PDX primary tumor burden study, WHIM2 single-cell suspensions in HF and Cultrex<sup>®</sup> BME (3432-005-01, R&D Systems, Minneapolis MN, USA) (500,000 cells / 100  $\mu$ L) were seeded unilaterally into the fourth mammary gland of NSG mice. After tumors reached an average size of 9 mm<sup>2</sup>, mice were treated with either vehicle (1% Methylcellulose + 0.1%

Tween 80, 3x per week), KPT-330 (5 mg/kg, 3 days per week) [29], Azelnidipine (3 mg/kg, 5x per week), Belinostat (60 mg/kg, 5x per week), Entrectinib (30 mg/kg, 5x per week) [66], Mefloquine (30 mg/kg, 5x per week) [67], and each single-agent's respective combination therapy with KPT-330 (3x per week). After the tumor burden was reached according to the animal use protocol or the tumor growth followed a particular trend (*e.g.*, no growth or shrinkage over time, observed continual growth, etc.), a particular group with the observed trend was euthanized. For all future *in vivo* primary tumor burden studies, WHIM2 or HCI-001 single-cell suspensions in HF and Cultrex® BME (3432-005-01, R&D Systems, Minneapolis MN, USA) (500,000 cells / 100 µL) were seeded unilaterally into the fourth mammary gland of NSG mice. After tumors reached an average size of 9 mm<sup>2</sup>, mice were treated with either vehicle (1% Methylcellulose + 0.1% Tween 80, 3x per week), KPT-330 (5 mg/kg, 3x per week) [29], everolimus (10 mg/kg, 3x per week) [54], or KPT-330 (5 mg/kg) + everolimus (10 mg/kg) (3x per week) combination. After the tumor burden was reached (~256 mm<sup>2</sup>) or the tumor growth followed a particular trend, a particular group with the observed trend was euthanized. At the end of each study, all tumor measurements were converted to tumor volume (mm<sup>3</sup>) with the formula  $V = \frac{L}{2} \times W^2$ , where  $V$  stands for tumor volume,  $L$  stands for tumor length and  $W$  stands for tumor width [68]. Tumors were subsequently cut into pieces, placed into microcentrifuge tubes, flash-frozen in dry ice, and stored at -80°C until further use.

#### *In vivo PDX metastasis burden studies*

WHIM2 single-cell suspensions in HF buffer + luciferin (500,000 cells / 100 µL) were injected intracardially into five-week old NSG mice. To ensure successful intracardiac injection, the injected mice were immediately imaged with the IVIS® Spectrum In Vivo Imaging System (4382250, Revvity, Waltham MA, USA). Radiance in the head of the mouse and throughout the mouse's body indicated a successful injection. The radiance in the chest area only indicated an unsuccessful injection. Unsuccessfully injected mice were euthanized immediately. WHIM2-intracardiac-injected mice were treated with either vehicle (1% Methylcellulose + 0.1% Tween 80, 3x per week), KPT-330 (5 mg/kg, 3x per week) [29], everolimus (10 mg/kg, 3x per week) [54] or KPT-330 (5 mg/kg) + everolimus (10 mg/kg) (3x per week) combination starting from seven days post-injection. Additionally, for all future *in vivo* PDX metastasis studies, once a week mice were injected with 200 µL filtered luciferin intraperitoneally and incubated for five minutes, after which they were IVIS imaged to observe metastasis progression. After four weeks of treatment, mice were injected with 200 µL filtered luciferin intraperitoneally each and euthanized after five minutes of incubation. Then, the brains, livers, ovaries, and lungs were excised from the mice and imaged in the IVIS. After imaging, all organ groups were normalized to each other to quantify metastasis presence and burden in each treatment group based on organ location.

#### *Hematoxylin & eosin staining of PDX model sections*

PDX sections paraffinized to glass slides were placed on a heat block at 60°C for one hour. Then the slides were subjected to incubation in xylene twice for two minutes, then rehydrated by the following incubations: twice in 100% EtOH for two minutes, once in 95% EtOH for two minutes, and then once in dH<sub>2</sub>O for one minute. Then, the slides were incubated in Gill #3 100%

Hematoxylin (GHS332, Sigma-Aldrich, St. Louis MO, USA) for five minutes, and then washed in tap water for one minute. Afterwards, the slides were incubated in acid alcohol (400 mL 70% EtOH + 1 mL HCl) for one minute, followed by a one-minute washing in tap water. The slides were blued in Scott's Tap Water for one minute, and then rinsed in 95% EtOH for one minute. After a 10-second incubation in Eosin, the slides were dehydrated in the following order: once in 95% EtOH for one minute, twice in 100% EtOH for one minute, and then twice in xylene for two minutes. Finally, coverslips were mounted onto the slides with Fisher Chemical™ Permount® (SP15, Fisher Scientific, Geel Belgium), dried overnight, and imaged with a Carl Zeiss™ AxioLab™ A1 light microscope and processed with ZEN Digital Imaging for Light Microscopy, a user interface software for Carl Zeiss light microscopy imaging systems (RRID:SCR\_013672).

### *Immunohistochemical staining of PDX model sections*

PDX sections paraffinized to glass slides were placed on a heat block at 60°C for one hour. The slides were subjected to incubation in xylene twice for two minutes, then rehydrated by the following incubations: twice in 100% EtOH for two minutes, once in 95% EtOH for two minutes, once in 70% EtOH for two minutes, and then once in dH<sub>2</sub>O for one minute. Subsequently, the slides were incubated in a coplin jar containing retrieval buffer (Tris-EDTA pH 9.0) and incubated in a decloaking chamber under pressure until the chamber reached 125°C. Once the chamber dropped to normal pressure, the slides were removed from the retrieval buffer and cooled in TBST for at least 30 seconds. A hydrophobic pen was used to draw around the individual PDX sections on the glass slides, and then 100 µL peroxidase block (K4011, Dako North America Inc., Carpinteria CA, USA) was applied to each section for five minutes. During blocking, rabbit 1° antibody was made at the desired titers and kept on ice until further use. After blocking, the slides were briefly washed in TBST and placed in a humidified chamber. Then, the desired 100 µL rabbit 1° antibody diluted in SignalStain® Antibody Diluent (8112, Cell Signaling Technology, Danvers MA, USA) (Table 2) was applied to each PDX section and incubated in the humidified chamber overnight at 4°C. The next day, the 1° antibody was tapped off and the slides were washed three times in TBST for five minutes each. Afterwards, 100 µL polymer/HRP 2° antibody (K4011, Dako North America Inc., Carpinteria CA, USA) was applied to each PDX section and incubated at RT for 20 minutes. While washing with TBST, DAB working solution was prepared by adding one drop DAB+ chromogen per 1 mL DAB+ substrate buffer (K4011, Dako North America Inc., Carpinteria CA, USA). After the TBST washing, 100 µL DAB working solution was applied to each PDX section for exactly 10 minutes. DAB working solution was then decanted into the appropriate waste container, upon which the slides were washed in TBST for one minute and then immersed in Gill #3 100% Hematoxylin (GHS332, Sigma-Aldrich, St. Louis MO, USA) for exactly 10 seconds followed by three washings in tap water for 10 seconds each. PDX sections were dehydrated in the following order: once in 70% EtOH for one minute, once in 95% EtOH for one minute, twice in 100% EtOH for five minutes each, then twice in xylene for five minutes each. After dehydration, coverslips were mounted with Fisher Chemical™ Permount® (SP15, Fisher Scientific, Geel, Belgium) onto the PDX slides, dried overnight, and imaged with a Carl Zeiss™ AxioLab™ A1 light microscope and processed with ZEN Digital Imaging for Light Microscopy, a user interface software for Carl Zeiss light microscopy imaging systems (RRID:SCR\_013672).



All IHC images were quantified for optical density (OD) in ImageJ via the *Color Deconvolution* method and by using the equation  $OD = \log \left( \frac{255}{\text{mean intensity}} \right)$  [69].

**Table 2: 1° antibodies used for IHC experiments.**

Protein Target	Isotype	Reactivity	kDa	Dilution	Company	Catalog Number
XPO1	Rabbit IgG	H, M, Mk	123	1:200	Cell Signaling Technology	#46429
FKBP1A	Rabbit IgG	H, M	12	1:500	Novus Biologicals	#NB300-508

#### *Nuclear fractionation of flash-frozen primary mammary gland tumor*

Nuclear fractionation of flash-frozen tissue was performed according to and with the Active Motif® Nuclear Extract Kit protocol (40010, Active Motif, Carlsbad CA, USA). This protocol assumes 1000 mg of tissue is to be used. For different tissue amounts, the amounts of buffer should be adjusted according to the manufacturer's instructions. Flash-frozen tissue stored at -80°C was crushed with a mortar and pestle in liquid nitrogen. On ice, 3 mL ice-cold 1X hypotonic buffer containing phosphatase and protease inhibitors with DTT and detergent supplementation was added to the powdered tissue in a Dounce homogenizer and homogenized with a large-clearance pestle for 20 strokes to disrupt tissue into a single-cell slurry. To ensure the cells were dissociated, a small sample was analyzed under a microscope before proceeding. After incubating on ice for 15 minutes, the slurry was centrifuged for 10 minutes at 850 G at 4°C. Proceeding with cytoplasmic fraction collection, the supernatant was discarded and the cells were resuspended in 500 µL 1X hypotonic buffer, transferred to a pre-chilled microcentrifuge tube, and incubated for 15 minutes on ice. Then, 25 µL detergent was added and the sample was vortexed for 10 seconds at the highest setting. Before proceeding with centrifugation, the cell suspension was checked under a microscope to ensure lysis occurred and that nuclei have been released. If lysis occurred, the sample was centrifuged for 30 seconds at 14,000 G at 4°C. The cytoplasmic supernatant was transferred into a new pre-chilled microcentrifuge tube and stored at -80°C until further use. The nuclear pellet was then resuspended in 50 µL complete lysis buffer and then vortexed for 10 seconds at the highest setting. Subsequently, the sample was incubated for 30 minutes on ice on a rocking platform set to 150 rpm. Afterwards, the sample was vortexed for 30 seconds at the highest setting and then centrifuged for 10 minutes at 14,000 G at 4°C. Finally, the nuclear supernatant was aliquoted into microcentrifuge tubes and stored at -80°C until further use, while avoiding freeze/thaw cycles.

#### *Bradford assay & SDS-PAGE sample preparation*

The following 1 mL BSA standards were made from 2 mg/mL BSA stock in ddH<sub>2</sub>O: Blank (ddH<sub>2</sub>O only, A), 1 µg/µL (B), 2 µg/µL (C), 4 µg/µL (D), 8 µg/µL (E), 10 µg/µL (F), 15 µg/µL (G), and 20 µg/µL (H). 200 µL of Bradford reagent (500-0006, Bio-Rad, Hercules CA, USA) was added to

each standard solution, mixed thoroughly and pop spun. Then, each standard was added to its own cuvettes and placed in the BioMate™ 160 UV-Vis Spectrophotometer (840-301000, ThermoFisher, Waltham MA, USA). The *Bradford* program was selected along with the *8-sample rotation* function. Then, the blank and BSA standards were scanned. While scanning, the sample solutions were prepared (800  $\mu$ L ddH<sub>2</sub>O + 1  $\mu$ L sample + 200  $\mu$ L Bradford reagent), mixed thoroughly, pop spun, and transferred to their respective cuvettes. After obtaining the absorbance values for the standards, all standards except for the blank standard were taken out and the respective sample cuvettes were placed into the spectrophotometer, upon which the spectrophotometer was run again and the absorbance values and protein concentrations of the samples were obtained from the spectrophotometer. When finished, the samples were discarded. After calculating the amount of sample to add to ddH<sub>2</sub>O and 4x sample buffer, which is prepared by adding 100  $\mu$ L  $\beta$ -mercaptoethanol (M6250, Sigma-Aldrich, St. Louis MO, USA) per 900  $\mu$ L 4x Laemmli Sample Buffer (1610747, Bio-Rad, Hercules CA, USA), the sample was mixed with the ddH<sub>2</sub>O and 4x sample buffer thoroughly, boiled on a heating block at 95°C for 10 minutes and then pop spun. Finally, the prepared loading samples were either used immediately for SDS-PAGE or stored at -20°C until further use. When the sample was taken out of -20°C storage, the sample was boiled at 95°C for 10 minutes before being used.

### *SDS-PAGE*

10-well 4-15% Mini-PROTEAN® TGX™ Precast Protein Gels (4561084, Bio-Rad, Hercules CA, USA) were set up in a Mini-PROTEAN® Tetra cell gel rig (1658040, Bio-Rad, Hercules CA, USA) and filled with 1X running buffer. After loading the respective amounts of protein ladder (1610374, Bio-Rad, Hercules CA, USA) and samples into their gel wells, the lid was placed onto the gel rig (red-to-red and black-to-black), and the gel was run at 100 V until the gel ladder began to resolve. Once the ladder was resolved, the voltage was increased to 120 V until the lowest ladder line reached the green bottom while ensuring the samples did not run off the gel.

### *Immunoblotting*

An Immobilon®-FL PVDF Membrane (IPFL00010, Millipore Sigma, Burlington MA, USA) and WypAll® X60 Cloths (34770, Kimberly-Clark Professional, Irving TX, USA) were cut to be slightly larger than the gel. Once the gel was finished running, the PVDF membrane was soaked in 100% MeOH to activate it. Meanwhile, the cloth layers were soaked in 1X transfer buffer. In the semi-dry Trans-Blot® Turbo™ Transfer System (1704150, Bio-Rad, Hercules CA, USA), seven pieces of pre-soaked cloth layers were placed in the cassette, rolled, and then flattened with a roller to get out any bubbles. The PVDF membrane was rinsed in 1X transfer buffer and flattened on top of the cloth layers in the cassette. Then, the finished gel was taken out of the rig, trimmed accordingly with a razor blade, and placed on top of the PVDF membrane. Finally, seven more pieces of pre-soaked cloths were placed on top of the gel and gently flattened to remove any further air bubbles. Then, the cassette was closed firmly with the lid locked and placed inside the semi-dry Transfer System. The machine was turned on and the *mini-gel* program was selected to run for 30 minutes, after which the membrane was taken out and placed immediately into 1X TBST. Afterwards, the membrane was soaked in Ponceau stain for five minutes to ensure the protein

transfer was successful. The membrane was washed in tap water briefly to remove the Ponceau solution, and then blocked in Intercept® (TBS) Blocking Buffer (927-60001, LI-COR Biosciences, Lincoln NE, USA) for one hour at room temperature, and then rinsed in 1X TBST. Meanwhile, respective 1° Rabbit antibodies were prepared in Intercept® (TBS) Blocking Buffer (Table 3). Once the rinsing was complete, the membrane was incubated with its respective 1° antibody overnight at 4°C on a rocker or for two hours at room temperature. After removing the 1° antibody and storing it at 4°C until further use, the membrane was washed with 1X TBST. Then, 2° Donkey anti-Rabbit IRDye® 680RD antibody (926-68073, LI-COR Biosciences, Lincoln NE, USA) was diluted 1:10,000 in Intercept® (TBS) Blocking Buffer and incubated with the membrane for one hour at room temperature covered in aluminum foil. The 2° antibody was discarded, and the membrane was washed in 1X TBST. The membrane was imaged in the Odyssey® Fc Imaging System with the software Image Studio™ Lite (LI-COR Biosciences, Lincoln NE, USA). The 600 nm channel was imaged for 30 seconds, and the 700 nm channel was imaged for two minutes and five seconds.

**Table 3: 1° antibodies used for immunoblotting diluted in Intercept® (TBS) Blocking Buffer.**

Protein Target	Isotype	Reactivity	kDa	Dilution	Company	Catalog Number
XPO1	Rabbit IgG	H, M, Mk	123	1:1000	Cell Signaling Technology	#46429
FKBP1A	Rabbit IgG	H, M, R	12	1:500	Cell Signaling Technology	#55104
Survivin	Rabbit IgG	H, M, R	16	1:1000	Cell Signaling Technology	#2808
Cyclin D1	Rabbit IgG	H, M, R	36	1:500	Cell Signaling Technology	#2978
rpS6	Rabbit IgG	H, M, R, Mk	32	1:1000	Cell Signaling Technology	#2217
phospho-rpS6	Rabbit IgG	H, M, R, Mk, Mi, Sc	32	1:2000	Cell Signaling Technology	#4858
H3	Rabbit IgG	H, M, R, Mk, Z, B, Pg	17	1:1000	Cell Signaling Technology	#9715
$\alpha/\beta$ Tubulin	Rabbit IgG	H, M, R, Mk, ZF, B	55, 52	1:1000	Cell Signaling Technology	#2148

### *Statistical analyses*

For the preliminary *in vitro* studies conducted by Tia H. Turner, unpaired student's t-tests were used to determine the statistical significance of differences in cell viability between control and

drug-treated conditions *in vitro*;  $p < 0.05$  was considered statistically significant. Data are presented as means  $\pm$  standard deviations where appropriate.

For *in vivo* studies, one-way ANOVA was used to determine the statistical significance of tumor volume differences between the vehicle control and drug-treated tumors at the vehicle endpoint, and one-way ANOVA was also used to determine the statistical significance of tumor volume differences between the KPT-330 + everolimus combination-treated groups and single-agent-treated groups;  $p < 0.05$  was considered statistically significant. Two-tailed heteroscedastic student's t-tests were used to determine the statistical significance of differences in the optical density of protein between two PDXs *in vitro*;  $p < 0.05$  was considered statistically significant. *R* version 4.2.3 was used to conduct statistical analyses.

## Results

### Identification of FKBP1A as a biomarker for mTORC1 activity in TNBC

After the preliminary *in vivo* trial with KPT-330 in combination with Azelnidipine, Entrectinib, Mefloquine, and Belinostat resulting in non-significant effects on tumor burden compared to KPT-330 alone (Figure 5), we sought to revisit our *in vitro* analysis for suitable drugs to pair with KPT-330 as BBB-permeable compounds. We noted that Rapamycin displayed similarly promising responses *in vitro* (Figure 1; Figure 2). Therefore, we decided to pursue its second-generation derivative everolimus. Since both Rapamycin and everolimus target FKBP1A, an activator of mTORC1, before pursuing *in vitro* testing, we analyzed our TNBC bulk and single-cell RNAseq datasets (Figure 7).

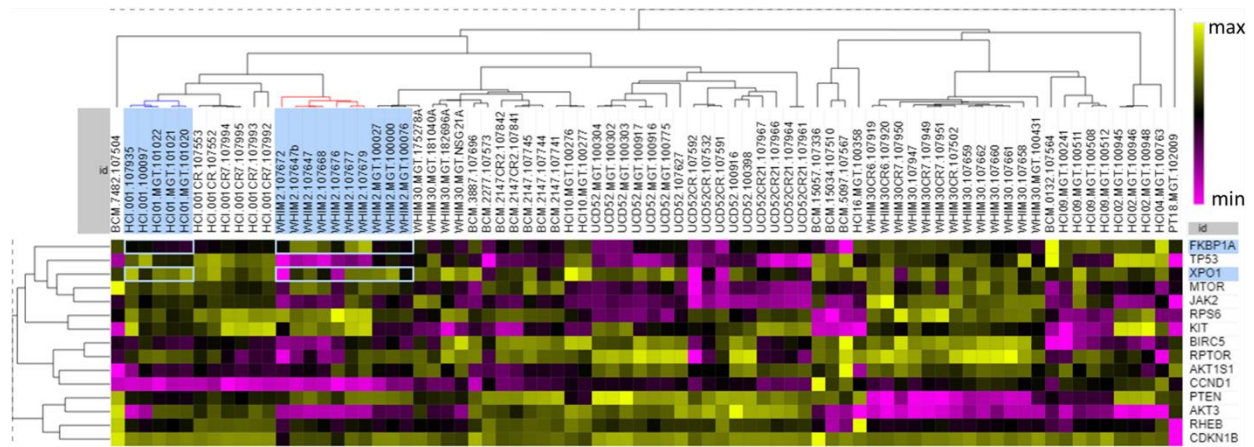


**Figure 7: Bulk RNA-seq TPM expression analysis of KPT-330 and everolimus protein targets and downstream affected proteins.** FKBP1A & XPO1 are highlighted with HCI-001 (blue branches) and WHIM2 (red branches). The minimum TPM expression is approaching pink and the maximum TPM expression is approaching yellow.

The above bulk RNA-seq heatmap depicts the transcript per million (TPM) expression of XPO1 (target of KPT-330), FKBP1A (target of everolimus), and downstream affected proteins (Figure 7). XPO1 expression is increased in all TNBCs except for UCD52CR and PT18, whereas FKBP1A expression is increased in BCM7482, WHIM2, HCI-010, WHIM30CR, WHIM30, BCM-0532, HCI-009, HCI-002 and HCI-004 (Figure 7). On the other hand, XPO1 expression is decreased in WHIM2, UCD52CR and PT18. FKBP1A expression is the lowest in HCI-001, HCI-001CR, WHIM30, BCM-2147, UCD52CR and PT18 (Figure 7). This indicates that while XPO1 expression seems equally distributed in TNBC PDXs with minor exceptions, FKBP1A is unequally expressed among the TNBC PDXs, with some expressing greater amounts of FKBP1A compared to others. As such, it is apparent that some TNBC PDXs are FKBP1A-low and FKBP1A-high.

After analyzing our bulk RNA-seq data, we proceeded to analyze our single-cell RNA-seq data to assess if the same observations hold true at the single-cell level (Figure 8).

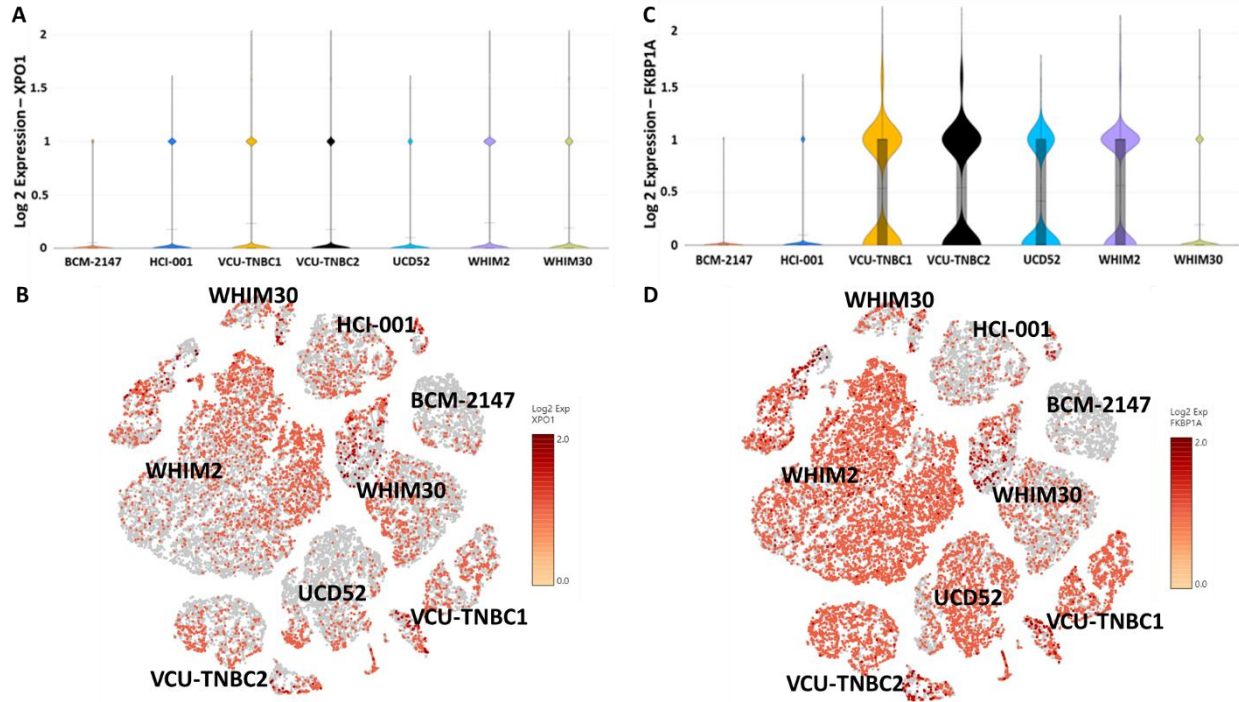


**Figure 8: Single-cell RNA-seq expression analysis of KPT-330 and everolimus protein targets and downstream affected proteins.** Using historical scRNA-seq data, log 2 expression of XPO1 in a violin plot (A) and t-SNE (B) and log 2 expression of FKBP1A in a violin plot (C) and t-SNE (D) were generated for various TNBC PDXs: BCM-2147 (orange), HCI-001 (dark blue), VCU-TNBC1 (yellow), VCU-TNBC2 (black), UCD52 (light blue), WHIM2 (lavender) and WHIM30 (light green).

The violin plot for log 2 XPO1 expression shows the relationship of XPO1 expression to TNBC PDX type (Figure 8A). The box plot elements show that the median log 2 XPO1 expressions between each TNBC PDX are similar, and the shape of distribution being the widest at 1 unit of log 2 XPO1 expression indicates XPO1 expression in these TNBCs are concentrated around the median, thereby suggesting that the expression of XPO1 in these PDXs are similar. This is supported by t-SNE clustering of log 2 XPO1 expression in these PDXs (Figure 8B). Intriguingly, all TNBCs except for UCD52, WHIM30, and BCM-2147 form distinct subpopulations.

As for the violin plot for log 2 FKBP1A expression, which shows the relationship of FKBP1A expression to TNBC PDX type (Figure 8C), the box plot elements of this violin plot show the median log 2 FKBP1A expressions of VCU-TNBC1, VCU-TNBC2, UCD52, and WHIM2 are greater than those of BCM-2147, HCI-001 and WHIM30. The distribution shape of VCU-TNBC1, VCU-TNBC2, UCD52, and WHIM2 being wider in the middle and bottom end of the violin compared to BCM-2147, HCI-001 and WHIM30 indicates that log 2 FKBP1A expression has a higher probability of being concentrated near the median in VCU-TNBC1, VCU-TNBC2, UCD52 and WHIM2 (Figure 8C). This is echoed by t-SNE clustering of log 2 FKBP1A expression in these PDXs (Figure 8D). In conclusion, while log 2 XPO1 expression appears similar in all TNBC PDXs, log 2 FKBP1A expression is higher in some TNBC PDXs compared to others, suggesting that FKBP1A could serve as a biomarker in some TNBCs.

Observing that FKBP1A could potentially be pursued as a biomarker based on our RNA-seq data, we wanted to verify this using an *in vitro* analysis of formalin-fixed paraffin-embedded



(FFPE) patient-derived xenografts (PDXs) of WHIM2 and HCI-001 as representatives for their respective high and low transcriptomic expressions of FKBP1A (Figure 9).

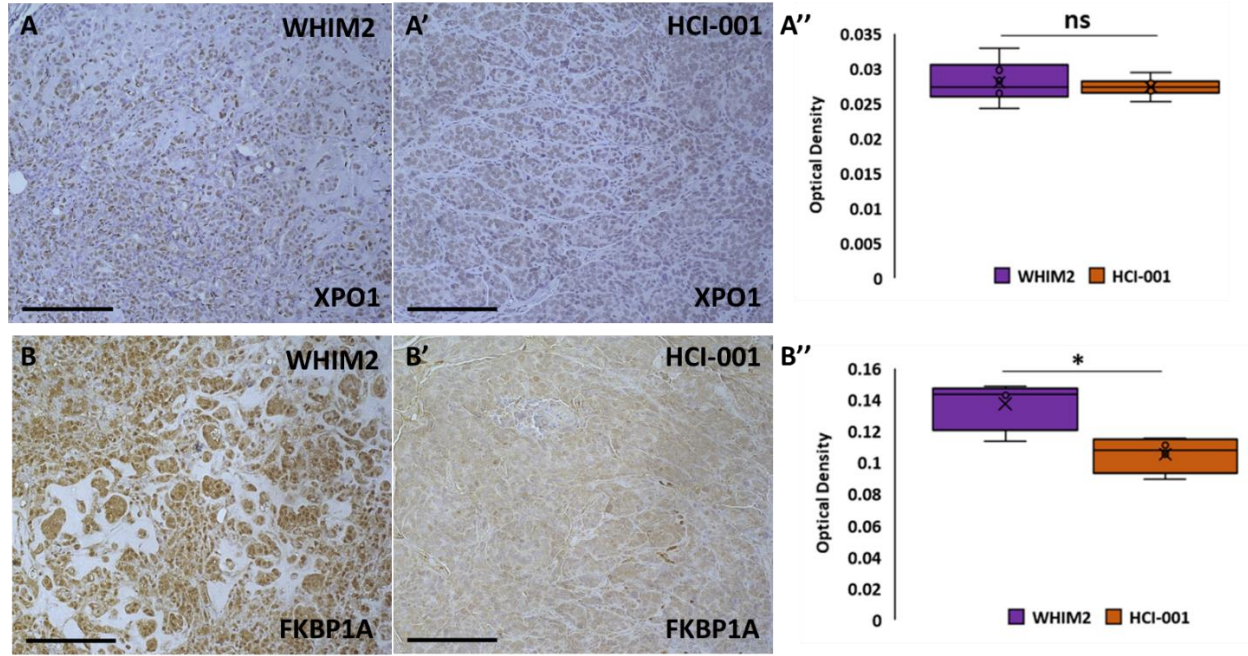


**Figure 9: Validation of XPO1 expression in WHIM2 and HCI-001 PDX tissue and increased FKBP1A expression in WHIM2 compared to HCI-001.** XPO1 IHC staining in (A) WHIM2 FFPE and (A') HCI-001 FFPE. (A'') Quantification of XPO1 optical density and comparison between WHIM2 and HCI-001 (n = 6, Student's t-test, two-tailed, heteroscedastic,  $p > 0.05$ , ns). FKBP1A IHC staining in (B) WHIM2 FFPE and (B') HCI-001 FFPE. (B'') Quantification of FKBP1A optical density and comparison between WHIM2 and HCI-001 (n = 4, Student's t-test, two-tailed, heteroscedastic,  $p < 0.05$ , \*). Scalebars represent 200  $\mu$ m.

XPO1 expression in WHIM2 and HCI-001 appear overall similar and homogeneous throughout the tissue (Figure 9A&A'). As expected, the DAB staining of the anti-XPO1 antibody resides in the nuclei of each of the cells, indicating that XPO1 is present in the nucleus. To quantify protein from these IHC images, they need to be converted to an 8-bit image and then converted to a final value known as optical density. The optical density describes a sample's ability to absorb a given amount of light, which allows us to quantify any given amount of protein, in this case with ImageJ. Here, there was no significant difference in the optical densities of XPO1 in WHIM2 and HCI-001, suggesting that the total amount of XPO1 in WHIM2 and HCI-001 are similar (Figure 9A'').

On the other hand, the cytoplasmic FKBP1A, while homogeneous in its expression in both WHIM2 and HCI-001, presents itself with stronger brown staining in WHIM2 (Figure 9B). In HCI-001, its appearance is fainter (Figure 9B'). Indeed, when quantified through ImageJ, FKBP1A has a significantly higher optical density in WHIM2 than in HCI-001 (Figure 9B''). The data suggest that FKBP1A is more highly expressed in WHIM2 than in HCI-001, which is further supported by the bulk and single-cell RNA-seq data. As such, TNBCs appear to greatly differ in their genomic landscape due to their differing expressions of FKBP1A, and therefore their mTOR activity.

### *KPT-330 + everolimus reduces mTORC1-overactive primary MGT burden*

We, therefore, confirmed that FKBP1A could be utilized as a biomarker for the treatment of TNBC. Moving forward with WHIM2 (FKBP1A-high) as our selected model of interest, we sought to answer if KPT-330 in combination with everolimus could serve as a strong candidate for the treatment of FKBP1A-high, and therefore mTORC1-overactive TNBC. To do this, we decided to test this therapy for WHIM2 and compare it to a FKBP1A-low PDX *in vivo*, namely HCI-001.

To utilize our human PDXs *in vivo*, they were grown in NSG mice because they lack a functional adaptive immune system [55]. As previously described, the PDX cell suspensions were injected into the fourth mammary gland of each mouse, and after reaching a sufficient size ( $\sim 9 \text{ mm}^2$ ) the mice were treated with their respective drugs or vehicle control (Figure 10).

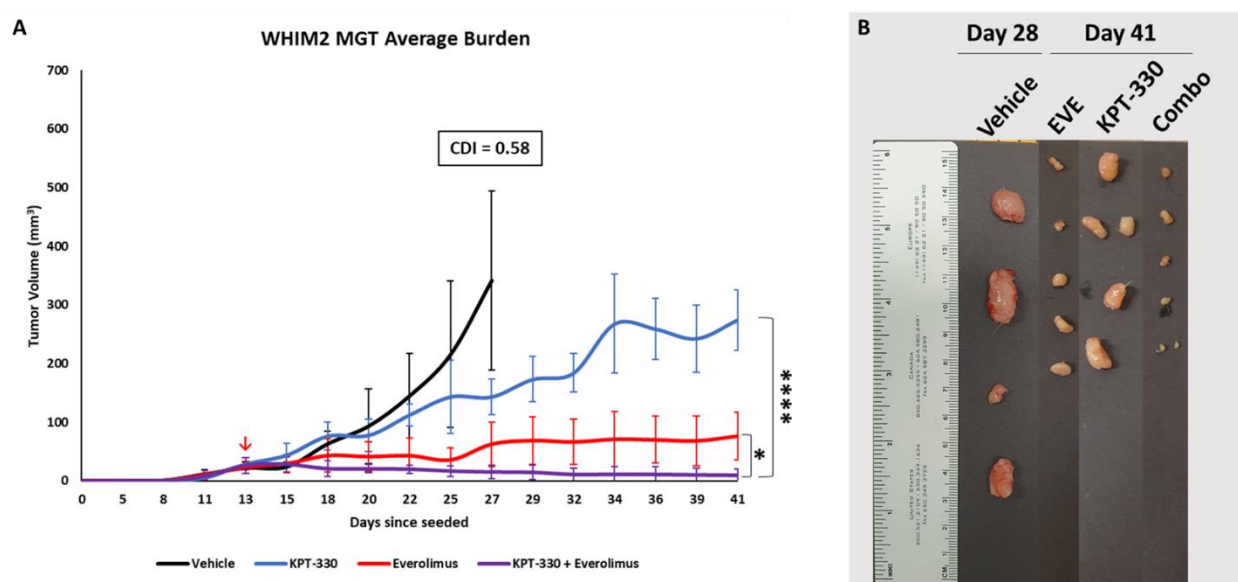


**Figure 10: *In vivo* assessment of average WHIM2 MGT burden over time after treatment with therapy.** (A) *In vivo* tumor burden after treatment with vehicle (black,  $n = 4$ ), KPT-330 (blue,  $n = 4$ ), everolimus (red,  $n = 5$ ) or KPT-330 + everolimus (purple,  $n = 5$ ). Tumor burden is measured as tumor volume (y-axis,  $\text{mm}^3$ ) by days since seeded (x-axis). Treatments started on day 13 since seeded (red arrow).  $\text{CDI} < 0.7$  was considered to indicate synergistic drug activity, and one-way ANOVA was performed to assess differences in tumor volume between KPT-330 + everolimus treatment group and the single-agent treatment groups, where  $p < 0.05$  was considered statistically significant. (B) Excised tumor masses on respective days of final treatment. Final days of treatment were day 28 since seeded for vehicle and day 41 since seeded for KPT-330, everolimus and KPT-330 + everolimus (Combo). A ruler is next to the tumors to evaluate the final tumor size. To assess the toxicity of the compounds, the mice were weighed over time (Supplementary Figure 7).

As outlined in Figure 10, treatments for the WHIM2-burdened mice began 13 days after being seeded. WHIM2 grows more aggressively compared to most other TNBC PDX models [58], and as such the vehicle-treated mice succumbed to WHIM2 tumor burden on day 28 (Figure 10A&B). Notably, the CDI was less than 0.7 at the vehicle endpoint for the KPT-330 + everolimus combination treatment compared to all other treatment groups, indicating that there was at least a negative additive effect of MGT burden when KPT-330 + everolimus was administered to WHIM2-burdened mice (Figure 10A). The KPT-330-treated tumors began to increase in volume over time, whereas the everolimus-treated tumors increased slightly between days 25 and 27, and



then plateaued below  $100 \text{ mm}^3$  for the rest of the study (Figure 10A). Meanwhile, tumors that were treated with KPT-330 + everolimus did not surpass  $50 \text{ mm}^3$  and remained near-palpable until the end of the study. The study was ended at day 41 due to the observable trends that KPT-330-treated and even everolimus-treated WHIM2 tumors would eventually grow through the treatment, whereas KPT-330 + everolimus-treated WHIM2 tumors would remain near-palpable (Figure 10A&B). Furthermore, both the everolimus-treated and KPT-330 + everolimus-treated tumors were much smaller in size compared to the vehicle-treated and KPT-330-treated tumors when measured with a ruler (Figure 10B). We conclude that KPT-330 + everolimus has the potential to make a significant impact against mTORC1-overactive TNBCs. The evidence suggests that everolimus has an additive effect on reducing the WHIM2 tumor burden in combination with KPT-330.

Observing that this treatment was effective *in vivo* in the FKBP1A-high WHIM2, we sought to analyze its effectiveness *in vivo* in the FKBP1A-low HCI-001 in NSG mice (Figure 11).

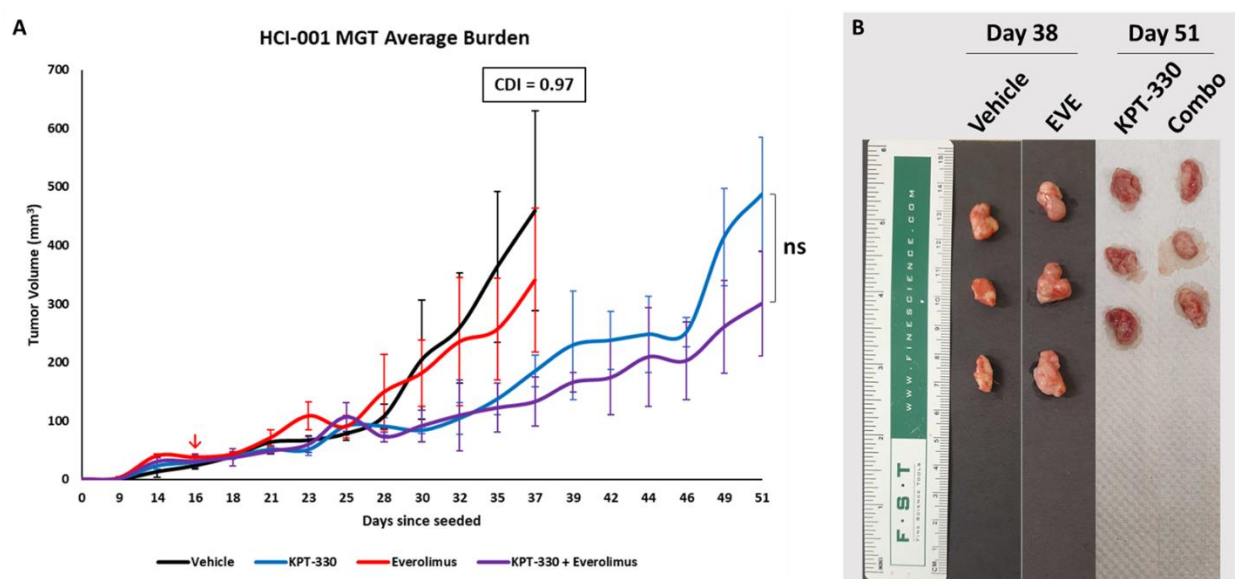


**Figure 11: *In vivo* assessment of average HCI-001 MGT burden over time after treatment with therapy.** (A) *In vivo* tumor burden after treatment with vehicle (black), KPT-330 (blue), everolimus (red), or KPT-330 + everolimus (purple), with  $n = 3$  per group. Tumor burden is measured as tumor volume (y-axis,  $\text{mm}^3$ ) by days since seeded (x-axis). Treatments started on day 16 since seeded (red arrow).  $\text{CDI} < 0.7$  was considered to indicate synergistic drug activity and one-way ANOVA was performed to assess differences in tumor volume between KPT-330 + everolimus treatment group and the single-agent treatment groups, where  $p < 0.05$  was considered statistically significant. (B) Excised tumor masses on respective days of final treatment. The final days of treatment were day 38 since seeded for vehicle and everolimus and day 51 since seeded for KPT-330 and KPT-330 + everolimus (Combo). A ruler is next to the tumors to evaluate the final tumor size. To assess the toxicity of the compounds, the mice were weighed over time (Supplementary Figure 8).

Treatments for the HCI-001-burdened mice began 16 days after being seeded, as HCI-001 grows more slowly than WHIM2 [58]. Both the vehicle-treated and everolimus-treated mice succumbed to HCI-001 tumor burden on day 38 (Figure 11). The CDI at the vehicle endpoint was greater than 0.7 for the KPT-330 + everolimus combination treatment compared to all other treatment groups, indicating that there was no synergistic impact for MGT burden when KPT-330 + everolimus was administered to HCI-001-burdened mice (Figure 11A). Despite this, the KPT-330-treated and

KPT-330 + everolimus-treated tumors continued with treatment after day 38. They began to increase in volume over time for the rest of the study. After continuing in this trend until day 51, the study was terminated (Figure 11). At the final endpoint of the study, the tumor sizes of the KPT-330-treated and KPT-330 + everolimus-treated tumors were comparable to the sizes of the vehicle-treated and everolimus-treated tumors from the vehicle endpoint when measured with a ruler (Figure 11B). Therefore, we conclude that KPT-330 + everolimus does not have the potential to make a significant impact against mTORC1-underactive TNBCs. The evidence suggests that KPT-330 likely drives the phenotype of treatment efficacy in HCI-001 TNBC PDXs, therefore indicating that everolimus has no significant effect on HCI-001 tumor burden.

*KPT-330 + everolimus reduces mTORC1-overactive metastasis burden in vivo*

Next, we examined if KPT-330 + everolimus treatment is effective in treating mTORC1-overactive TNBC breast-to-brain metastasis since both KPT-330 and everolimus are able to cross the BBB. Along these lines, we also wanted to observe if this treatment is also effective in other metastatic niches in other organs, such as the ovaries, liver, and lungs. As such, we injected luciferase-positive WHIM2 PDX cells intracardially into five-week-old NSG mice, and after seven days of waiting for the mice to recover and form metastases, the mice were treated three times a week for four weeks with vehicle, KPT-330, everolimus or the KPT-330 + everolimus combination. At the end of this study (day 35 since seeded), mice were first injected with luciferin, and after five minutes were imaged with the IVIS to observe the total metastases formed in the mice and the effects of each of the drugs on these metastatic niches (Figure 12).

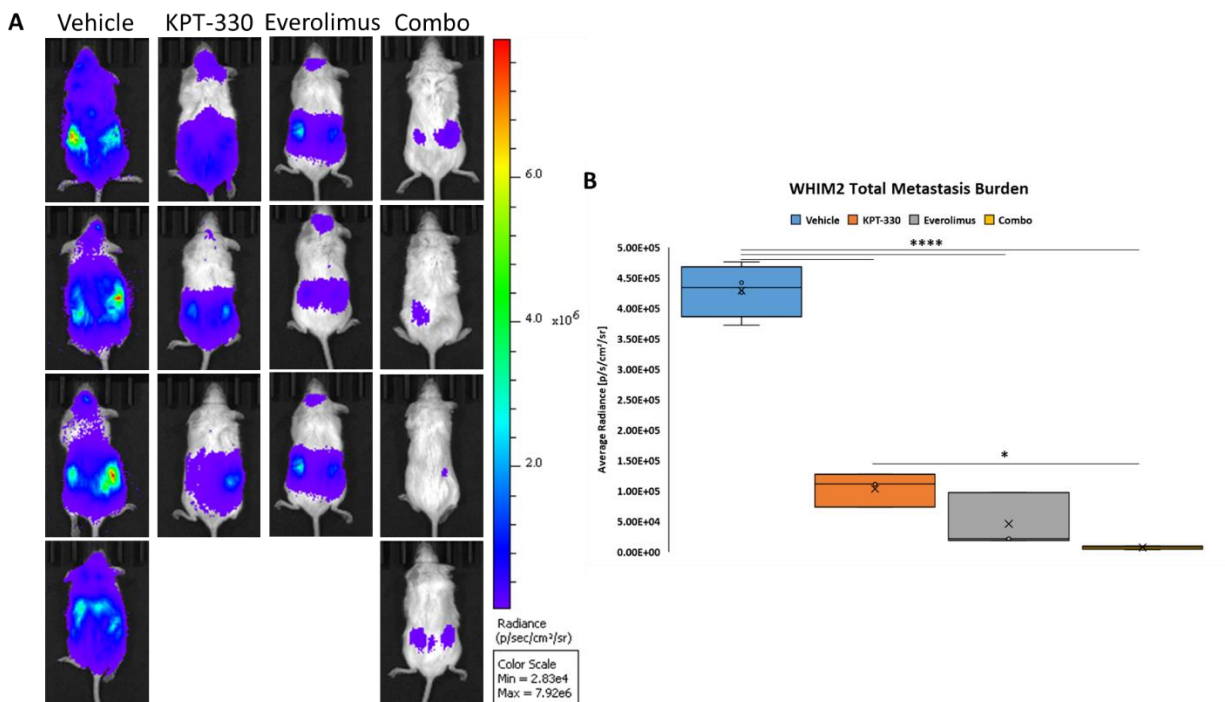


**Figure 12: *In vivo* assessment of average WHIM2 total metastasis burden at day 35 since seeding after four weeks of treatment with therapy.** (A) IVIS images of luciferin-cleaved radiance (p/sec/cm<sup>2</sup>/sr) in NSG mice burdened with WHIM2 metastasis at day 35 since intracardiac injection. Mice were treated either with vehicle (n = 4), KPT-330 (n = 3), everolimus (n = 3), or Combo (n = 4). A radiance scalebar next to the images depicts radiance intensity, with red depicting the highest radiance and purple depicting the lowest radiance. (B) Box and whisker plot of average radiances (p/sec/cm<sup>2</sup>/sr) of total WHIM2 metastasis burden in vehicle, KPT-330, everolimus, and Combo mice. One-way ANOVA was performed to assess differences in total metastasis burden represented by average radiance between the vehicle group and the treatment groups, where  $p < 0.05$  was considered statistically significant. To assess the toxicity of the compounds, the mice were weighed over time (Supplementary Figure 9). Total metastasis burden over time in all mice can be seen in Supplementary Figure 10.

Total metastasis burden was observed in all mice at day 35 since intracardiac injection with WHIM2 PDX cells (Figure 12A). Notably in the dorsal view, the vehicle-treated mice had intense red and green radiance in their lower abdomens, indicating the presence of large ovary metastases (Figure 12A; vehicle). There were also dark blue and light blue signals in the chest area of these mice, which were interpreted as lung and liver metastases. Finally, brain metastases were also present, as can be seen by the dark blue clusters of radiance in the head of each of the mice. These signals were noticeably weaker in the KPT-330-treated and everolimus-treated mice, although the signals derived from the brain and ovary metastases were still visible (Figure 12A; KPT-330, everolimus). However, in the KPT-330 + everolimus-treated mice (from now on referred to as Combo), there was a clear absence of signal from the brain, lung, and liver regions, with a dark blue to purple signal in either of the ovaries (Figure 12A; Combo).

After imaging, the radiance of the metastases in the mice was quantified and their radiances were averaged and plotted in a box-and-whisker plot to compare the average radiance intensities between the vehicle-treated group and the KPT-330-treated, everolimus-treated, and Combo-treated groups (Figure 12B). The vehicle-treated metastases were significantly more radiant than the KPT-330-treated ( $p < 0.0001$ ), everolimus-treated ( $p < 0.0001$ ), and Combo-treated metastases

( $p < 0.0001$ ), which suggests that the treatments were effective in reducing total metastasis burden. Additionally, KPT-330-treated metastases were significantly more radiant than the Combo-treated metastases ( $p < 0.05$ ), indicating that receiving KPT-330 + everolimus treatment has a significantly more negative effect on metastasis than receiving KPT-330 treatment alone.

Then, the mice were euthanized and the brains, ovaries, livers, and lungs were excised from the mice and imaged in the IVIS as well to detect organ-specific metastatic niches and to evaluate the specific effectiveness of the administered drugs to these metastases (Figures 13-16).

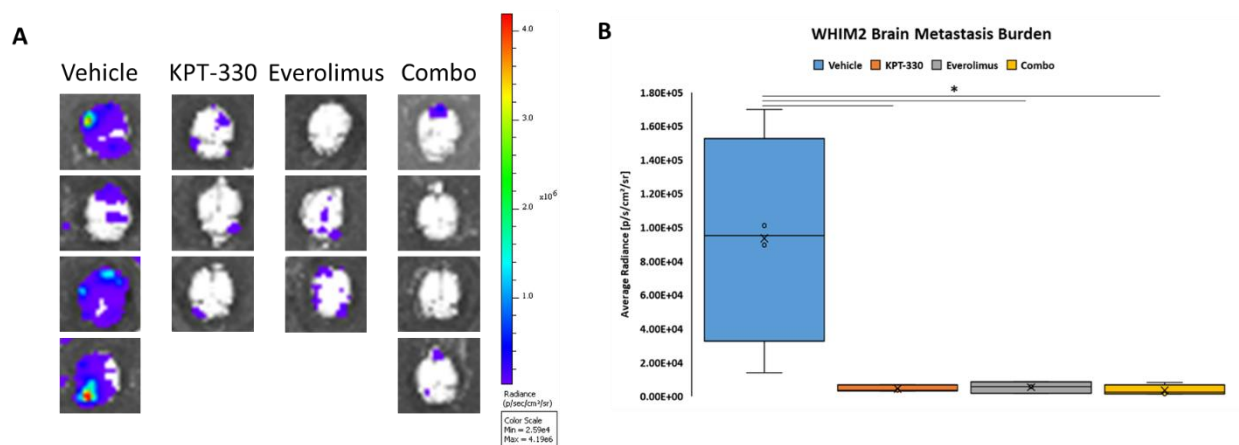


**Figure 13: Ex vivo assessment of average WHIM2 brain metastasis burden at day 35 since seeding after four weeks of treatment with therapy.** (A) IVIS images of luciferin-cleaved radiance (p/sec/cm<sup>2</sup>/sr) in excised mouse brains burdened with WHIM2 metastasis at day 35 since intracardiac injection. Mice were treated either with vehicle (n = 4), KPT-330 (n = 3), everolimus (n = 3), or Combo (n = 4). A radiance scalebar next to the images depicts radiance intensity, with red depicting the highest radiance and purple depicting the lowest radiance. (B) Box and whisker plot of average radiances (p/sec/cm<sup>2</sup>/sr) of WHIM2 brain metastasis burden in vehicle, KPT-330, everolimus and Combo mouse brains. One-way ANOVA was performed to assess differences in brain metastasis burden represented by average radiance between the vehicle group and the treatment groups, where  $p < 0.05$  was considered statistically significant.

First, WHIM2 brain metastasis burden was observed in all excised brains (Figure 13A). The vehicle-treated brains overall had areas of intense green and red radiance in either the frontal lobe or the cerebellum (Figure 13A; vehicle). These signals were dark blue in the KPT-330-treated, everolimus-treated and Combo-treated brains, indicating less WHIM2 metastatic niches were in the brain (Figure 13A; KPT-330, everolimus, Combo).

When quantified, it became clear that the vehicle-treated WHIM2 brain metastases were significantly more radiant than the KPT-330-treated ( $p < 0.05$ ), everolimus-treated ( $p < 0.05$ ) and Combo-treated WHIM2 brain metastases ( $p < 0.05$ ), suggesting that the treatments were effective in reducing brain metastasis burden compared to the vehicle control (Figure 13B). However, there was no significant difference in average radiance between the KPT-330-treated, everolimus-treated and Combo-treated brains. The data suggests that KPT-330 does not need to be paired with everolimus to reduce WHIM2 brain metastasis burden, as the single agents are effective enough to reduce WHIM2 brain metastasis burden (Figure 13B).

Despite this observation in the brain, metastases in the other organs were affected differently, namely the ovary metastases harbored a unique response to the treatments (Figure 14).

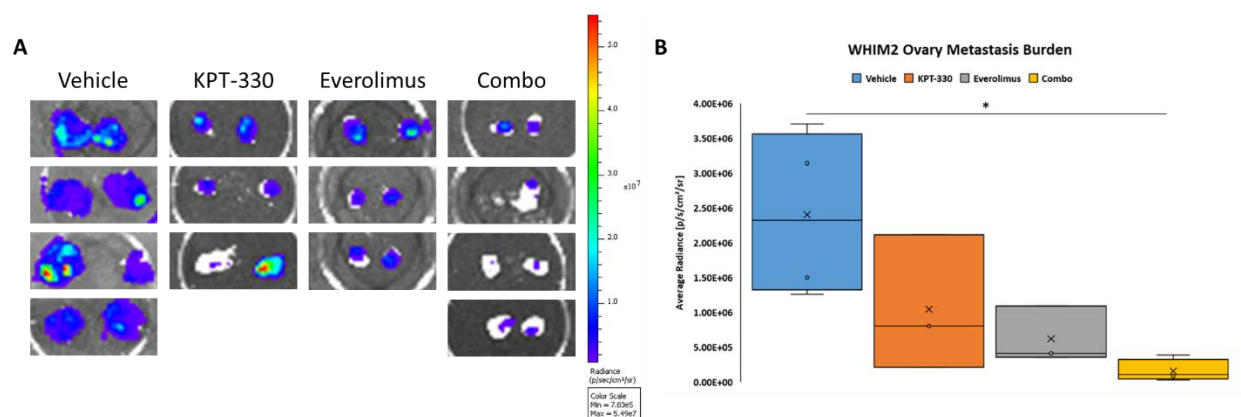


**Figure 14: Ex vivo assessment of average WHIM2 ovary metastasis burden at day 35 since seeding after four weeks of treatment with therapy.** (A) IVIS images of luciferin-cleaved radiance (p/sec/cm<sup>2</sup>/sr) in excised mouse ovaries burdened with WHIM2 metastasis at day 35 since intracardiac injection. Mice were treated either with vehicle (n = 4), KPT-330 (n = 3), everolimus (n = 3), or Combo (n = 4). A radiance scalebar next to the images depicts radiance intensity, with red depicting the highest radiance and purple depicting the lowest radiance. (B) Box and whisker plot of average radiances (p/sec/cm<sup>2</sup>/sr) of WHIM2 ovary metastasis burden in vehicle, KPT-330, everolimus, and Combo mouse ovaries. One-way ANOVA was performed to assess differences in ovary metastasis burden represented by average radiance between the vehicle group and the treatment groups, where  $p < 0.05$  was considered statistically significant.

WHIM2 ovary metastasis burden was observed in all excised ovaries (Figure 14A). The vehicle-treated ovaries were not only noticeably larger than the average mouse ovary, but were comprised entirely with light blue, green, yellow, and red radiance, indicating the presence of WHIM2 metastases throughout the entirety of the ovaries (Figure 14A; vehicle). These signals were dark blue and green in the KPT-330-treated and everolimus-treated ovaries, with one of the KPT-330-treated ovaries having intense red radiance. This indicated that despite treatment with either KPT-330 or everolimus, the ovary metastases were still largely present (Figure 14A; KPT-330, everolimus). Meanwhile, in the Combo-treated ovaries, there was largely no radiance present except for slight dark blue and light blue radiance in the centers of the ovaries (Figure 14A; Combo). This suggests that there was less WHIM2 metastatic burden in the Combo-treated ovaries compared to the vehicle-treated ovaries.

This observation became evident when the radiances of the ovaries were quantified (Figure 14B). vehicle-treated WHIM2 ovary metastases were only significantly more radiant than the Combo-treated WHIM2 ovary metastases ( $p < 0.05$ ), but there was no significant difference in average radiance between the vehicle-treated WHIM2 ovary metastases and the KPT-330-treated and everolimus-treated WHIM2 ovary metastases. This suggests that only the Combo treatment was effective in reducing ovary metastasis burden compared to the vehicle control (Figure 14B). The data suggests that it is vital to pair KPT-330 with everolimus to reduce WHIM2 ovary metastasis burden, as the single agents were not effective enough to reduce WHIM2 ovary metastasis burden compared to the vehicle-treated group.

Next, we observed metastatic burden in the liver (Figure 15).

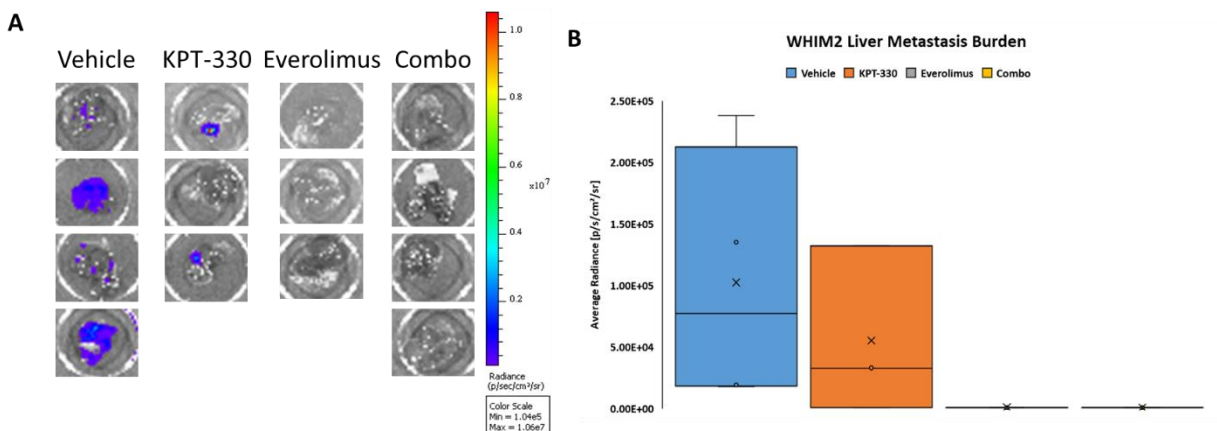


**Figure 15: *Ex vivo* assessment of average WHIM2 liver metastasis burden at day 35 since seeding after four weeks of treatment with therapy.** (A) IVIS images of luciferin-cleaved radiance (p/sec/cm<sup>2</sup>/sr) in excised mouse livers burdened with WHIM2 metastasis at day 35 since intracardiac injection. Mice were treated either with vehicle (n = 4), KPT-330 (n = 3), everolimus (n = 3), or Combo (n = 4). A radiance scalebar next to the images depicts radiance intensity, with red depicting the highest radiance and purple depicting the lowest radiance. (B) Box and whisker plot of average radiances (p/sec/cm<sup>2</sup>/sr) of WHIM2 liver metastasis burden in vehicle, KPT-330, everolimus, and Combo mouse ovaries. One-way ANOVA was performed to assess differences in liver metastasis burden represented by average radiance between the vehicle group and the treatment groups, where  $p < 0.05$  was considered statistically significant.

WHIM2 liver metastasis burden was observed in some of the excised livers (Figure 15A). Notably, compared to the vehicle-treated and KPT-330-treated livers, the everolimus-treated and Combo-treated livers did not express any radiance, suggesting that WHIM2 liver metastases were not present in these two treatment groups (Figure 15A; everolimus, Combo). On the other hand, only two of the three KPT-330-treated livers expressed dark-blue radiance (Figure 15A; KPT-330), and two of the four vehicle-treated livers expressed dark-blue radiance, with the other two containing purple puncta of radiance throughout the liver (Figure 15A; vehicle), suggesting that these livers received some metastases sporadically.

When the radiances of the livers were quantified, it became apparent that there was no significant difference in radiance between the vehicle-treated livers and the livers treated with either KPT-330, everolimus, or both (Figure 15B). This suggests that KPT-330 + everolimus are not sufficient to treat TNBC liver metastases.

Lastly, the efficacy of KPT-330 + everolimus was observed in the lungs (Figure 16).



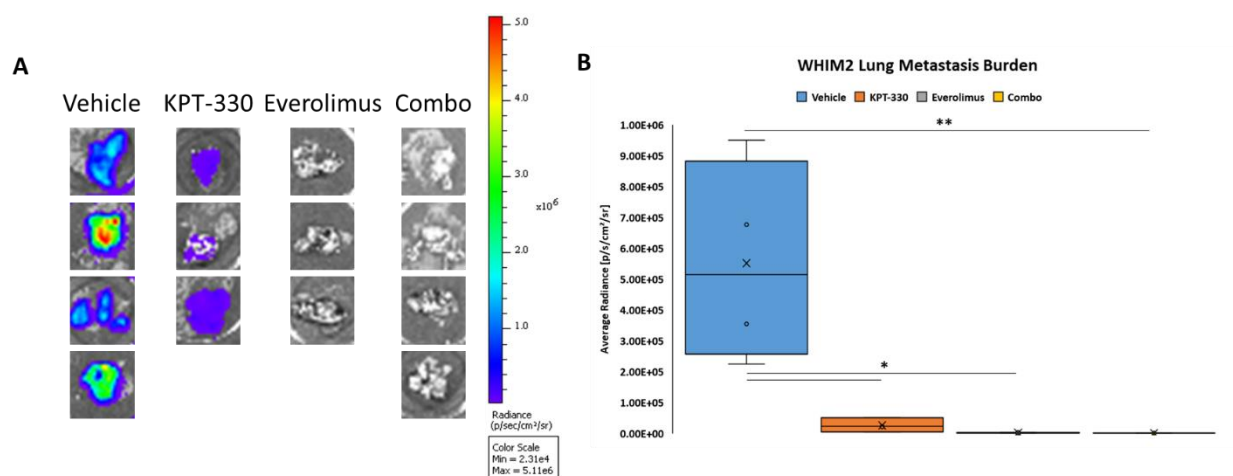


**Figure 16: Ex vivo assessment of average WHIM2 lung metastasis burden at day 35 since seeding after four weeks of treatment with therapy.** (A) IVIS images of luciferin-cleaved radiance (p/sec/cm<sup>2</sup>/sr) in excised mouse lungs burdened with WHIM2 metastasis at day 35 since intracardiac injection. Mice were treated either with vehicle (n = 4), KPT-330 (n = 3), everolimus (n = 3), or Combo (n = 4). A radiance scalebar next to the images depicts radiance intensity, with red depicting the highest radiance and purple depicting the lowest radiance. (B) Box and whisker plot of average radiances (p/sec/cm<sup>2</sup>/sr) of WHIM2 lung metastasis burden in vehicle, KPT-330, everolimus, and Combo mouse ovaries. One-way ANOVA was performed to assess differences in lung metastasis burden represented by average radiance between the vehicle group and the treatment groups, where  $p < 0.05$  was considered statistically significant.

WHIM2 lung metastasis burden was observed in all excised lungs except for the everolimus and Combo groups (Figure 16). The vehicle-treated lungs range from dark blue radiance all the way to red radiance (Figure 16A; vehicle), while the KPT-330-treated lungs only express blue radiance (Figure 16A; KPT-330). This suggests that KPT-330 was effective in reducing radiance, and therefore metastasis, in the lungs compared to the vehicle. Contrary to the KPT-330-treated lungs, both the everolimus-treated and Combo-treated lungs express no radiance when compared to the vehicle-treated lungs, implying that both everolimus and the Combo treatments were effective in nullifying the radiance emitted by the lung metastases compared to the vehicle (Figure 16A; vehicle, everolimus, Combo). This overall suggests that there was less WHIM2 metastatic burden in the KPT-330-treated, everolimus-treated, and Combo-treated lungs compared to the vehicle-treated lungs.

This observation is confirmed via quantification of the lung metastases (Figure 16B). While vehicle-treated lungs were significantly more radiant than the KPT-330-treated ( $p < 0.05$ ) and the everolimus-treated lungs ( $p < 0.05$ ), but even more so significantly radiant than the Combo-treated lungs ( $p < 0.01$ ). This suggests that the Combo treatment was more effective in reducing lung metastasis burden compared to the KPT-330 single agent and everolimus single agent (Figure 16B). The data suggests that KPT-330 + everolimus is necessary to reduce WHIM2 lung metastasis burden. In conclusion, KPT-330 + everolimus is a promising combination therapy for the treatment of mTORC1-overactive TNBC brain, ovary, and lung metastasis.

#### *Combination therapy reduces phosphorylation of rpS6 and attenuates Survivin*

To understand how this combination therapy was killing the WHIM2 PDX cells *in vivo*, treated primary mammary gland tumors at the end of each study were harvested from the mice and

fractionated for their cytoplasmic and nuclear lysates, respectively, to detect the effects of KPT-330 and everolimus on the tumor signaling pathways (Figure 17).

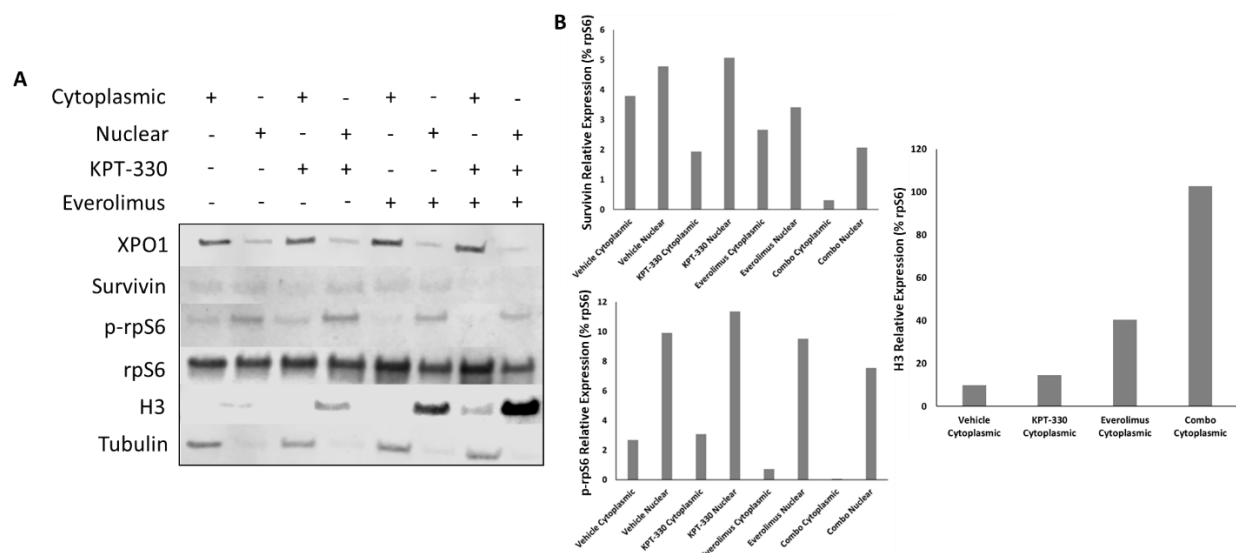


**Figure 17: Immunoblot of WHIM2 mammary tumors.** (A) Each lane was subjected to four conditions of lysate: Cytoplasmic, Nuclear, KPT-330-treated (5 mg/kg), and everolimus-treated (10 mg/kg). + indicated the presence of a given condition, and - indicated the lack of a given condition. H3 was stained for as a nuclear loading control, whereas Tubulin was stained for as a cytoplasmic loading control. Primary antibody information and titers can be found in Table 2. (B) Quantification of XPO1, Survivin, phospho-rpS6, H3, and Tubulin relative to rpS6 [% rpS6] in cytoplasmic and nuclear lysates treated either with vehicle, KPT-330, everolimus, or both drugs.

In the WHIM2 lysates, dark XPO1 bands were observable in the cytoplasmic fractions of all lysates. Faint Survivin bands were present both the cytoplasmic and nuclear lysates except for the Combo-treated lysates, where no Survivin bands were present. This suggests that upon treatment with KPT-330 and everolimus, Survivin was attenuated (Figure 17A). Strong rpS6 bands were present in both the cytoplasmic and nuclear fractions of all treatment groups, however, phospho-rpS6 bands were observed in all cytoplasmic and nuclear fractions of all treatment groups except for the cytoplasmic everolimus-treated and Combo-treated lysates (Figure 17A). Relative to rpS6 expression, XPO1 was expressed at similar levels in the cytoplasm (~20-30%) and nucleus (~5%) in under all treatment conditions, respectively (Fig. 17B). As expected, there was a trend of Survivin being retained more in the nuclear fractions compared to the control when treated with KPT-330 or combo, with combo-treated lysates also expressing less Survivin in the cytoplasm (< 1%) and nucleus (~2%) compared to all other treatment groups (Fig. 17B). This trend was also apparent for phospho-rpS6. Interestingly, H3 expression relative to rpS6 expression in the nucleus increased upon treatment with combo (Fig. 17B). H3 is a histone that compacts DNA with other histones in the nucleus to form chromatin [70]. Upon treatment with KPT-330 + everolimus, the phosphorylation of rpS6 is reduced, the nuclear export of Survivin is downregulated, Survivin is downregulated, and H3 is overexpressed (Fig. 8). H3 overexpression has been previously shown to be cytotoxic and alter chromatin structure [71]. The reduction of phosphorylation of rpS6 indicates that mTORC1 is being inhibited, thus allowing for apoptotic signaling to occur [47], and the attenuation of Survivin compounded with its build-up in the nucleus indicates mechanistic action of both everolimus and KPT-330.



## Discussion

KPT-330 is currently FDA approved for adult patients with relapsed or refractory multiple myeloma (RRMM), albeit in combination with bortezomib and dexamethasone [72]. KPT-330 has also shown prior promise *in vitro* and *in vivo* as an effective treatment for several cancers, such as breast cancer, sarcoma and prostate cancer [29, 38, 73]. In the clinic, KPT-330 has mild adverse effects in patients, including decreased appetite, vomiting and weight loss [74]. Everolimus is FDA approved for the treatment of SEGA [46]. Everolimus was also shown in a phase III ER+ breast cancer clinical trial to enhance the efficacy of Exemestane in reducing tumor burden [75]. Everolimus has mild adverse effects in patients and clinical trials including stomatitis, rash, fatigue, anemia, and thrombocytopenia [53]. In rare cases, everolimus and other mTOR inhibitors can cause hyperglycemia because they negatively affect insulin metabolism [76, 77]. KPT-330 in combination with everolimus has been previously evaluated in non-Hodgkin lymphoma and was moderately effective *in vitro* and *in vivo* [78]. Despite the adverse effects of these compounds, their protein targets are abundant at the transcriptomic and proteomic level. This led us to hypothesize that KPT-330 + everolimus would prove itself as an effective treatment for FKBP1A-high TNBCs (Figure 7-9).

The FKBP1A-high WHIM2 reduced significantly in volume upon treatment with KPT-330 + everolimus *in vivo* compared to the FKBP1A-low HCI-001 (Figure 11 & 12), indicating that the effectiveness of everolimus is dependent on the presence of FKBP1A at the protein level. This tumor volume reduction is then further increased by the presence of KPT-330 due to the expression of XPO1 in TNBC. Additionally, the reduction in tumor volume suggests that KPT-330 and everolimus are bioavailable enough in the body to have an impact on tumor volume and burden. In future, more FKBP1A-high TNBC PDXs should be tested *in vivo* with this drug combination to solidify this finding. Of note, HCI-010, HCI-002, HCI-004, and WHIM30 are prime candidates according to our transcriptomic analyses (Figure 7). In addition, since this therapy is more effective in reducing tumor burden in the FKBP1A-high WHIM2 TNBC (Figure 10), FKBP1A should be considered as a biomarker for personalized TNBC treatment. In the clinic, a patient's tumor could be biopsied and then genetically assessed for FKBP1A upregulation, upon which they could receive KPT-330 + everolimus as a personalized therapy. This avenue of personalized therapy, known as pharmacogenomics, is widely used in the clinic to help target a variety of cancers for patients harboring key genes and mutations [79]. Because FKBP1A is not present as a biomarker in FKBP1A-low TNBCs, KPT-330 + everolimus would not be a viable personalized treatment option for FKBP1A-low TNBCs (Figure 11).

It is evident that KPT-330 and everolimus are able to cross the BBB due to the significant reduction in WHIM2 brain metastatic burden compared to the vehicle control (Figure 13). Despite the KPT-330 single agent, everolimus single agent, and Combo treatment statistically having the same efficacy in reducing WHIM2 brain metastases (Figure 13), it can be concluded that KPT-330 + everolimus is still a more suitable therapeutic option due to its significant action in reducing total metastatic burden (Figure 12), ovary metastatic burden (Figure 14), and lung metastatic burden (Figure 16). On the other hand, WHIM2 liver metastases treated with KPT-330, everolimus, or both drugs were not significantly different in burden compared to the vehicle-treated control. This can be explained by previous studies, which note that WHIM2 does not consistently seed the liver [58]. Using different FKBP1A-high, and therefore mTORC1-overactive TNBC PDXs for

metastasis experiments, such as HCI-010, HCI-002, HCI-004, and WHIM30, may yield different results for liver seeding and may provide insight on the effectiveness of KPT-330 + everolimus in FKBP1A-high TNBC liver metastasis burden.

The concentration of KPT-330 and everolimus in the brain remains unknown. To address this in future, liquid chromatography/mass spectrometry (LC/MS) will be utilized on FF brain tissue burdened with WHIM2 metastases to evaluate how much total KPT-330 and everolimus were able to cross the BBB and reach the brain. More specifically, LC/MS will provide insight into the drug concentration in the total brain. This will be useful to assess the efficacy of KPT-330 and everolimus in crossing the BBB. A variant of LC/MS, known as liquid chromatography/tandem mass spectrometry (LC/MS/MS) has previously been shown to accurately assess the concentration of drugs and other analytes in brain homogenate [80], solidifying this as a method that can be used to determine the concentration of drugs in the brain, and even other organs, after treatment.

Tolerance of therapeutic agents is an important factor in cancer therapy that must not be overlooked. If the applied treatment is too toxic to a patient, the side effects of the drug in the body may be fatal. Therefore, while conducting our *in vivo* studies with KPT-330 + everolimus, we closely assessed mouse body weight over the course of treatments. The average mouse body weight remained above 100% since the first day of measurement for WHIM2 primary tumor mice (Supplementary Figure 7), HCI-001 primary tumor mice (Supplementary Figure 8), and WHIM2 metastasis mice (Supplementary Figure 9) over the course of treatments. This indicated that KPT-330 supplemented with everolimus is possibly non-toxic to mice, thus being well-tolerated *in vivo*.

A recent study has shown that Survivin is attenuated by mTOR inhibition [81], which provides a possible interaction between the mechanisms of action of KPT-330 and everolimus in FKBP1A-high TNBC (Figure 17). Given that cytoplasmic Survivin is an indicator for poor prognosis in cancer, nuclear Survivin build-up via the inhibition of XPO1 by KPT-330 therefore has a negative effect on tumor survival [38]. This is then further compounded by the inactivation of FKBP1A by everolimus, which in turn inactivates mTORC1 and further attenuates Survivin. Everolimus is shown to actively suppress tumor survival through the downregulation of phospho-rpS6 and attenuation of Survivin in everolimus-treated and Combo-treated lysate (Figure 17). This suggests that everolimus is working as designed. Future experiments should stain for the presence of  $\gamma$ H2Ax, caspase 3, cleaved caspase 3, and more cargo proteins such as p53 to further demonstrate the apoptotic activity of KPT-330 and everolimus which can be deduced from *in vitro* (Figure 10) and *in vivo* (Figure 10-16) studies.

One future direction of this project is to assess the efficacy of KPT-330 + everolimus in chemotherapy-resistant TNBC primary tumor and metastatic disease. In particular, the use of Carboplatin-resistant (CR) TNBC models would be utilized for this aim. This would address the treatment of TNBCs which have developed a resistance to commonly used chemotherapies over time, an issue which is prevalent in many patients [29]. Based on the bulk RNAseq analysis, WHIM30CR would be utilized for this aim due to its high transcriptomic expression of FKBP1A (Figure 7). Assessing everolimus' other target protein, HIF-1 $\alpha$ , as a potential biomarker for personalized treatment for TNBC is another future aim. Furthermore, newer TNBC subtyping approaches based on multi-omic analysis of key tumor survival pathways such as mTOR/PI3K

pathway or EGFR/MAPK pathway will be utilized to identify mTORC1-overactive TNBCs and further identify common, newer therapies for the treatment of this disease [82].

Overall, these findings have the potential to make significant translational impacts for patients with basal-like TNBC brain, ovary, and lung metastasis. Both KPT-330 and everolimus have already been shown to be well-tolerated in humans. Therefore, this drug combination may be expeditiously translated to the clinical setting.

## References

1. Perou, C. M., Sørlie, T., Eisen, M. B., van de Rijn, M., Jeffrey, S. S., Rees, C. A., Pollack, J. R., Ross, D. T., Johnsen, H., Akslen, L. A., Fluge, Ø., Pergamenschikov, A., Williams, C., Zhu, S. X., Lønning, P. E., Børresen-Dale, A.-L., Brown, P. O., & Botstein, D. (2000). Molecular portraits of human breast tumours. In *Nature* (Vol. 406, Issue 6797, pp. 747–752). Springer Science and Business Media LLC. <https://doi.org/10.1038/35021093>
2. Gote, V., Nookala, A. R., Bolla, P. K., & Pal, D. (2021). Drug Resistance in Metastatic Breast Cancer: Tumor Targeted Nanomedicine to the Rescue. In *International Journal of Molecular Sciences* (Vol. 22, Issue 9, p. 4673). MDPI AG. <https://doi.org/10.3390/ijms22094673>
3. Tavassoli, F. A. (1999). *Pathology of the Breast*. McGraw Hill Professional.
4. Ramos-Solis, N., & Yeh, E. S. (2022). Triple Negative Breast Cancer. In *Comprehensive Pharmacology* (pp. 35–48). Elsevier. <https://doi.org/10.1016/b978-0-12-820472-6.00056-6>
5. Lin, N. U., Vanderplas, A., Hughes, M. E., Theriault, R. L., Edge, S. B., Wong, Y.-N., Blayney, D. W., Niland, J. C., Winer, E. P., & Weeks, J. C. (2012). Clinicopathologic features, patterns of recurrence, and survival among women with triple-negative breast cancer in the National Comprehensive Cancer Network. In *Cancer* (Vol. 118, Issue 22, pp. 5463–5472). Wiley. <https://doi.org/10.1002/cncr.27581>
6. Rakha, E. A., Elsheikh, S. E., Aleskandarany, M. A., Habashi, H. O., Green, A. R., Powe, D. G., El-Sayed, M. E., Benhasouna, A., Brunet, J.-S., Akslen, L. A., Evans, A. J., Blamey, R., Reis-Filho, J. S., Foulkes, W. D., & Ellis, I. O. (2009). Triple-Negative Breast Cancer: Distinguishing between Basal and Nonbasal Subtypes. In *Clinical Cancer Research* (Vol. 15, Issue 7, pp. 2302–2310). American Association for Cancer Research (AACR). <https://doi.org/10.1158/1078-0432.ccr-08-2132>
7. Prat, A., Parker, J. S., Karginova, O., Fan, C., Livasy, C., Herschkowitz, J. I., He, X., & Perou, C. M. (2010). Phenotypic and molecular characterization of the claudin-low intrinsic subtype of breast cancer. In *Breast Cancer Research* (Vol. 12, Issue 5). Springer Science and Business Media LLC. <https://doi.org/10.1186/bcr2635>
8. Lehmann, B. D., Bauer, J. A., Chen, X., Sanders, M. E., Chakravarthy, A. B., Shyr, Y., & Pietenpol, J. A. (2011). Identification of human triple-negative breast cancer subtypes and preclinical models for selection of targeted therapies. In *Journal of Clinical Investigation* (Vol. 121, Issue 7, pp. 2750–2767). American Society for Clinical Investigation. <https://doi.org/10.1172/jci45014>
9. Liedtke, C., Mazouni, C., Hess, K. R., André, F., Tordai, A., Mejia, J. A., Symmans, W. F., Gonzalez-Angulo, A. M., Hennessy, B., Green, M., Cristofanilli, M., Hortobagyi, G. N., & Pusztai, L. (2008). Response to Neoadjuvant Therapy and Long-Term Survival in Patients With Triple-Negative Breast Cancer. In *Journal of Clinical Oncology* (Vol. 26, Issue 8, pp. 1275–1281). American Society of Clinical Oncology (ASCO). <https://doi.org/10.1200/jco.2007.14.4147>
10. Foulkes, W. D., Smith, I. E., & Reis-Filho, J. S. (2010). Triple-Negative Breast Cancer. In *New England Journal of Medicine* (Vol. 363, Issue 20, pp. 1938–1948). Massachusetts Medical Society. <https://doi.org/10.1056/nejmra1001389>

11. Kim, C., Gao, R., Sei, E., Brandt, R., Hartman, J., Hatschek, T., Crosetto, N., Foukakis, T., & Navin, N. E. (2018). Chemoresistance Evolution in Triple-Negative Breast Cancer Delineated by Single-Cell Sequencing. In *Cell* (Vol. 173, Issue 4, pp. 879-893.e13). Elsevier BV. <https://doi.org/10.1016/j.cell.2018.03.041>
12. Welch, D. R., & Hurst, D. R. (2019). Defining the Hallmarks of Metastasis. In *Cancer Research* (Vol. 79, Issue 12, pp. 3011–3027). American Association for Cancer Research (AACR). <https://doi.org/10.1158/0008-5472.can-19-0458>
13. Hunter, K. W., Crawford, N. P., & Alsarraj, J. (2008). Mechanisms of metastasis. In *Breast Cancer Research* (Vol. 10, Issue S1). Springer Science and Business Media LLC. <https://doi.org/10.1186/bcr1988>
14. Sullivan, N. J., Sasser, A. K., Axel, A. E., Vesuna, F., Raman, V., Ramirez, N., Oberyszyn, T. M., & Hall, B. M. (2009). Interleukin-6 induces an epithelial–mesenchymal transition phenotype in human breast cancer cells. In *Oncogene* (Vol. 28, Issue 33, pp. 2940–2947). Springer Science and Business Media LLC. <https://doi.org/10.1038/onc.2009.180>
15. Yin, L., Duan, J.-J., Bian, X.-W., & Yu, S. (2020). Triple-negative breast cancer molecular subtyping and treatment progress. In *Breast Cancer Research* (Vol. 22, Issue 1). Springer Science and Business Media LLC. <https://doi.org/10.1186/s13058-020-01296-5>
16. Harrell, J. C., Prat, A., Parker, J. S., Fan, C., He, X., Carey, L., Anders, C., Ewend, M., & Perou, C. M. (2011). Genomic analysis identifies unique signatures predictive of brain, lung, and liver relapse. In *Breast Cancer Research and Treatment* (Vol. 132, Issue 2, pp. 523–535). Springer Science and Business Media LLC. <https://doi.org/10.1007/s10549-011-1619-7>
17. Achrol, A. S., Rennert, R. C., Anders, C., Soffietti, R., Ahluwalia, M. S., Nayak, L., Peters, S., Arvold, N. D., Harsh, G. R., Steeg, P. S., & Chang, S. D. (2019). Brain metastases. In *Nature Reviews Disease Primers* (Vol. 5, Issue 1). Springer Science and Business Media LLC. <https://doi.org/10.1038/s41572-018-0055-y>
18. Feng, Y., Zhao, X., Lv, S., Xiong, B., Li, Y., & Zhang, M. (2020). Long disease-free survival (48 months) in a breast cancer patient with ovarian and pelvic metastasis—a case report. In *Translational Cancer Research* (Vol. 9, Issue 12, pp. 7669–7675). AME Publishing Company. <https://doi.org/10.21037/tcr-20-2031>
19. Turan, T., Aykan, B., Koc, S., Boran, N., Tulunay, G., Karacay, O., Erdogan, Z., & Kose, F. (2006). Analysis of Metastatic Ovarian Tumors from Extragenital Primary Sites. In *Tumori Journal* (Vol. 92, Issue 6, pp. 491–495). SAGE Publications. <https://doi.org/10.1177/030089160609200605>
20. Heitz, F., Harter, P., Lueck, H.-J., Fissler-Eckhoff, A., Lorenz-Salehi, F., Scheil-Bertram, S., Traut, A., & Bois, A. du. (2009). Triple-negative and HER2-overexpressing breast cancers exhibit an elevated risk and an earlier occurrence of cerebral metastases. In *European Journal of Cancer* (Vol. 45, Issue 16, pp. 2792–2798). Elsevier BV. <https://doi.org/10.1016/j.ejca.2009.06.027>
21. Heitz, F., Rochon, J., Harter, P., Lueck, H.-J., Fissler-Eckhoff, A., Barinoff, J., Traut, A., Lorenz-Salehi, F., & du Bois, A. (2011). Cerebral metastases in metastatic breast cancer: disease-specific risk factors and survival. In *Annals of Oncology* (Vol. 22, Issue 7, pp. 1571–1581). Elsevier BV. <https://doi.org/10.1093/annonc/mdq625>

22. Lin, N. U., Claus, E., Sohl, J., Razzak, A. R., Arnaout, A., & Winer, E. P. (2008). Sites of distant recurrence and clinical outcomes in patients with metastatic triple-negative breast cancer. In *Cancer* (Vol. 113, Issue 10, pp. 2638–2645). Wiley. <https://doi.org/10.1002/cncr.23930>
23. Niwińska, A., Murawska, M., & Pogoda, K. (2010). Breast cancer brain metastases: differences in survival depending on biological subtype, RPA RTOG prognostic class and systemic treatment after whole-brain radiotherapy (WBRT). In *Annals of Oncology* (Vol. 21, Issue 5, pp. 942–948). Elsevier BV. <https://doi.org/10.1093/annonc/mdp407>
24. Jin, J., Gao, Y., Zhang, J., Wang, L., Wang, B., Cao, J., Shao, Z., & Wang, Z. (2018). Incidence, pattern and prognosis of brain metastases in patients with metastatic triple negative breast cancer. In *BMC Cancer* (Vol. 18, Issue 1). Springer Science and Business Media LLC. <https://doi.org/10.1186/s12885-018-4371-0>
25. Morris, P. G., Murphy, C. G., Mallam, D., Accordini, M., Patil, S., Howard, J., Omuro, A., Beal, K., Seidman, A. D., Hudis, C. A., & Fournier, M. N. (2012). Limited Overall Survival in Patients with Brain Metastases from Triple Negative Breast Cancer. In *The Breast Journal* (Vol. 18, Issue 4, pp. 345–350). Hindawi Limited. <https://doi.org/10.1111/j.1524-4741.2012.01246.x>
26. Khawli, L. A., & Prabhu, S. (2013). Drug Delivery across the Blood–Brain Barrier. In *Molecular Pharmaceutics* (Vol. 10, Issue 5, pp. 1471–1472). American Chemical Society (ACS). <https://doi.org/10.1021/mp400170b>
27. Wilhelm, I., Molnár, J., Fazakas, C., Haskó, J., & Krizbai, I. (2013). Role of the Blood–Brain Barrier in the Formation of Brain Metastases. In *International Journal of Molecular Sciences* (Vol. 14, Issue 1, pp. 1383–1411). MDPI AG. <https://doi.org/10.3390/ijms14011383>
28. Turner, T. H., Alzubi, M. A., & Harrell, J. C. (2020). Identification of synergistic drug combinations using breast cancer patient-derived xenografts. In *Scientific Reports* (Vol. 10, Issue 1). Springer Science and Business Media LLC. <https://doi.org/10.1038/s41598-020-58438-0>
29. Rashid, N. S., Hairr, N. S., Murray, G., Olex, A. L., Leftwich, T. J., Gribble, J. M., Reed, J., Dozmorov, M. G., & Harrell, J. C. (2021). Identification of nuclear export inhibitor-based combination therapies in preclinical models of triple-negative breast cancer. In *Translational Oncology* (Vol. 14, Issue 12, p. 101235). Elsevier BV. <https://doi.org/10.1016/j.tranon.2021.101235>
30. Mahipal, A., & Malafa, M. (2016). Importins and exportins as therapeutic targets in cancer. In *Pharmacology & Therapeutics* (Vol. 164, pp. 135–143). Elsevier BV. <https://doi.org/10.1016/j.pharmthera.2016.03.020>
31. Cheng, Y., Holloway, M. P., Nguyen, K., McCauley, D., Landesman, Y., Kauffman, M. G., Shacham, S., & Altura, R. A. (2014). XPO1 (CRM1) Inhibition Represses STAT3 Activation to Drive a Survivin-Dependent Oncogenic Switch in Triple-Negative Breast Cancer. In *Molecular Cancer Therapeutics* (Vol. 13, Issue 3, pp. 675–686). American Association for Cancer Research (AACR). <https://doi.org/10.1158/1535-7163.mct-13-0416>

32. Senapedis, W. T., Baloglu, E., & Landesman, Y. (2014). Clinical translation of nuclear export inhibitors in cancer. In *Seminars in Cancer Biology* (Vol. 27, pp. 74–86). Elsevier BV. <https://doi.org/10.1016/j.semcancer.2014.04.005>
33. Kalid, O., Toledo Warshaviak, D., Shechter, S., Sherman, W., & Shacham, S. (2012). Consensus Induced Fit Docking (cIFD): methodology, validation, and application to the discovery of novel Crm1 inhibitors. In *Journal of Computer-Aided Molecular Design* (Vol. 26, Issue 11, pp. 1217–1228). Springer Science and Business Media LLC. <https://doi.org/10.1007/s10822-012-9611-9>
34. Lapalombella, R., Sun, Q., Williams, K., Tangeman, L., Jha, S., Zhong, Y., Goettl, V., Mahoney, E., Berglund, C., Gupta, S., Farmer, A., Mani, R., Johnson, A. J., Lucas, D., Mo, X., Daelemans, D., Sandanayaka, V., Shechter, S., McCauley, D., ... Byrd, J. C. (2012). Selective inhibitors of nuclear export show that CRM1/XPO1 is a target in chronic lymphocytic leukemia. In *Blood* (Vol. 120, Issue 23, pp. 4621–4634). American Society of Hematology. <https://doi.org/10.1182/blood-2012-05-429506>
35. Neggers, J. E., Vercruysse, T., Jacquemyn, M., Vanstreels, E., Baloglu, E., Shacham, S., Crochiere, M., Landesman, Y., & Daelemans, D. (2015). Identifying Drug-Target Selectivity of Small-Molecule CRM1/XPO1 Inhibitors by CRISPR/Cas9 Genome Editing. In *Chemistry & Biology* (Vol. 22, Issue 1, pp. 107–116). Elsevier BV. <https://doi.org/10.1016/j.chembiol.2014.11.015>
36. Abraham, S. A., & Holyoake, T. L. (2013). Redirecting traffic using the XPO1 police. In *Blood* (Vol. 122, Issue 17, pp. 2926–2928). American Society of Hematology. <https://doi.org/10.1182/blood-2013-09-523670>
37. Shafique, M., Ismail-Khan, R., Extermann, M., Sullivan, D., Goodridge, D., Boulware, D., Hogue, D., Soliman, H., Khong, H., & Han, H. S. (2019). A Phase II Trial of Selinexor (KPT-330) for Metastatic Triple-Negative Breast Cancer. In *The Oncologist* (Vol. 24, Issue 7, pp. 887–e416). Oxford University Press (OUP). <https://doi.org/10.1634/theoncologist.2019-0231>
38. Gravina, G. L., Mancini, A., Sanita, P., Vitale, F., Marampon, F., Ventura, L., Landesman, Y., McCauley, D., Kauffman, M., Shacham, S., & Festuccia, C. (2015). KPT-330, a potent and selective exportin-1 (XPO-1) inhibitor, shows antitumor effects modulating the expression of cyclin D1 and survivin in prostate cancer models. In *BMC Cancer* (Vol. 15, Issue 1). Springer Science and Business Media LLC. <https://doi.org/10.1186/s12885-015-1936-z>
39. Wettersten, H. I., Landesman, Y., Friedlander, S., Shacham, S., Kauffman, M., & Weiss, R. H. (2014). Specific Inhibition of the Nuclear Exporter Exportin-1 Attenuates Kidney Cancer Growth. In D. Chandra (Ed.), *PLoS ONE* (Vol. 9, Issue 12, p. e113867). Public Library of Science (PLOS). <https://doi.org/10.1371/journal.pone.0113867>
40. Talati, C., & Sweet, K. L. (2018). Nuclear transport inhibition in acute myeloid leukemia: recent advances and future perspectives. In *International Journal of Hematologic Oncology* (Vol. 7, Issue 3, p. IJH04). Future Medicine Ltd. <https://doi.org/10.2217/ijh-2018-0001>
41. Chang, H., Crochiere, M., Debler, S., Kashyap, T., Unger, T. J., Baloglu, E., Senapedis, W., Shacham, S., & Landesman, Y. (2019). Abstract 1998: Selinexor effectively inhibits tumor growth in a triple negative breast cancer brain metastasis mouse model. In *Cancer*

- Research (Vol. 79, Issue 13\_Supplement, pp. 1998–1998). American Association for Cancer Research (AACR). <https://doi.org/10.1158/1538-7445.am2019-1998>
42. Chou, T.-C. (2006). Theoretical Basis, Experimental Design, and Computerized Simulation of Synergism and Antagonism in Drug Combination Studies. In *Pharmacological Reviews* (Vol. 58, Issue 3, pp. 621–681). American Society for Pharmacology & Experimental Therapeutics (ASPET). <https://doi.org/10.1124/pr.58.3.10>
  43. Chou, T.-C. (2010). Drug Combination Studies and Their Synergy Quantification Using the Chou-Talalay Method. In *Cancer Research* (Vol. 70, Issue 2, pp. 440–446). American Association for Cancer Research (AACR). <https://doi.org/10.1158/0008-5472.can-09-1947>
  44. The Myeloma Beacon Staff. (2010, July 22). Bristol-Myers Squibb Halts Development of Tanespimycin [web log]. Retrieved June 27, 2023, from <https://myelomabeacon.org/news/2010/07/22/tanespimycin-development-halted/>.
  45. LoRusso, P. M. (2016). Inhibition of the PI3K/AKT/mTOR Pathway in Solid Tumors. In *Journal of Clinical Oncology* (Vol. 34, Issue 31, pp. 3803–3815). American Society of Clinical Oncology (ASCO). <https://doi.org/10.1200/jco.2014.59.0018>
  46. Krueger, D. A., Care, M. M., Holland, K., Agricola, K., Tudor, C., Mangeshkar, P., Wilson, K. A., Byars, A., Sahmoud, T., & Franz, D. N. (2010). Everolimus for Subependymal Giant-Cell Astrocytomas in Tuberous Sclerosis. In *New England Journal of Medicine* (Vol. 363, Issue 19, pp. 1801–1811). Massachusetts Medical Society. <https://doi.org/10.1056/nejmoa1001671>
  47. de la Cruz López, K. G., Toledo Guzmán, M. E., Sánchez, E. O., & García Carrancá, A. (2019). mTORC1 as a Regulator of Mitochondrial Functions and a Therapeutic Target in Cancer. In *Frontiers in Oncology* (Vol. 9). Frontiers Media SA. <https://doi.org/10.3389/fonc.2019.01373>
  48. Granata, S., Dalla Gassa, A., Carraro, A., Brunelli, M., Stallone, G., Lupo, A., & Zaza, G. (2016). Sirolimus and everolimus Pathway: Reviewing Candidate Genes Influencing Their Intracellular Effects. In *International Journal of Molecular Sciences* (Vol. 17, Issue 5, p. 735). MDPI AG. <https://doi.org/10.3390/ijms17050735>
  49. Alam, M. M., Fermin, J. M., Knackstedt, M., Noonan, M. J., Powell, T., Goodreau, L., Daniel, E. K., Rong, X., Moore-Medlin, T., Khandelwal, A. R., & Nathan, C.-A. O. (2023). Everolimus downregulates STAT3/HIF-1 $\alpha$ /VEGF pathway to inhibit angiogenesis and lymphangiogenesis in TP53 mutant head and neck squamous cell carcinoma (HNSCC). In *Oncotarget* (Vol. 14, Issue 1, pp. 85–95). Impact Journals, LLC. <https://doi.org/10.18632/oncotarget.28355>
  50. Naruse, T., Yanamoto, S., Yamada, S., Rokutanda, S., Kawakita, A., Kawasaki, G., & Umeda, M. (2015). Anti-Tumor Effect of the Mammalian Target of Rapamycin Inhibitor Everolimus in Oral Squamous Cell Carcinoma. In *Pathology & Oncology Research* (Vol. 21, Issue 3, pp. 765–773). Springer Science and Business Media LLC. <https://doi.org/10.1007/s12253-014-9888-1>
  51. Arango, N. P., Yuca, E., Zhao, M., Evans, K. W., Scott, S., Kim, C., Gonzalez-Angulo, A. M., Janku, F., Ueno, N. T., Tripathy, D., Akcakanat, A., Naing, A., & Meric-Bernstam, F. (2017). Selinexor (KPT-330) demonstrates anti-tumor efficacy in preclinical models of



- triple-negative breast cancer. In *Breast Cancer Research* (Vol. 19, Issue 1). Springer Science and Business Media LLC. <https://doi.org/10.1186/s13058-017-0878-6>
52. Martini, S., Zuco, V., Tortoreto, M., Percio, S., Campi, E., El Bezawy, R., Doldi, V., Landesman, Y., Pennati, M., & Zaffaroni, N. (2021). miR-34a-Mediated Survivin Inhibition Improves the Antitumor Activity of Selinexor in Triple-Negative Breast Cancer. In *Pharmaceuticals* (Vol. 14, Issue 6, p. 523). MDPI AG. <https://doi.org/10.3390/ph14060523>
  53. Paplomata, E., Zelnak, A., & O'Regan, R. (2013). Everolimus: side effect profile and management of toxicities in breast cancer. In *Breast Cancer Research and Treatment* (Vol. 140, Issue 3, pp. 453–462). Springer Science and Business Media LLC. <https://doi.org/10.1007/s10549-013-2630-y>
  54. Boyd, D. C., Zboril, E. K., Olex, A. L., Leftwich, T. J., Hairr, N. S., Byers, H. A., Valentine, A. D., Altman, J. E., Alzubi, M. A., Grible, J. M., Turner, S. A., Ferreira-Gonzalez, A., Dozmorov, M. G., & Harrell, J. C. (2023). Discovering Synergistic Compounds with BYL-719 in PI3K Overactivated Basal-like PDXs. In *Cancers* (Vol. 15, Issue 5, p. 1582). MDPI AG. <https://doi.org/10.3390/cancers15051582>
  55. Hudson, W., Li, Q., Le, C., & Kersey, J. (1998). Xenotransplantation of human lymphoid malignancies is optimized in mice with multiple immunologic defects. In *Leukemia* (Vol. 12, Issue 12, pp. 2029–2033). Springer Science and Business Media LLC. <https://doi.org/10.1038/sj.leu.2401236>
  56. Inotiv. WHIM2 PDX Models. Retrieved June 5, 2023, from <https://www.inotivco.com/whim-pdx-models>
  57. Baylor College of Medicine. Patient Information for Model: HCI-001. PDX Portal. Retrieved June 5, 2023, from <https://pdxportal.research.bcm.edu/pdxportal/model/HCI-001?dswid=-7307>
  58. Alzubi, M. A., Turner, T. H., Olex, A. L., Sohal, S. S., Tobin, N. P., Recio, S. G., Bergh, J., Hatschek, T., Parker, J. S., Sartorius, C. A., Perou, C. M., Dozmorov, M. G., & Harrell, J. C. (2019). Separation of breast cancer and organ microenvironment transcriptomes in metastases. In *Breast Cancer Research* (Vol. 21, Issue 1). Springer Science and Business Media LLC. <https://doi.org/10.1186/s13058-019-1123-2>
  59. Andrews, S. FastQC: A Quality Control Tool for High throughput Sequence Data. 2010. Volume 5, no. 1. 2019. Available online: <http://www.bioinformatics.babraham.ac.uk/projects/fastqc/> (accessed on 26 June 2023).
  60. Martin, M. Cutadapt removes adapter sequences from high-throughput sequencing reads. *EMBnet. J.* 2011, 17, 10–12.
  61. Dobin, A., Davis, C. A., Schlesinger, F., Drenkow, J., Zaleski, C., Jha, S., Batut, P., Chaisson, M., & Gingeras, T. R. (2012). STAR: ultrafast universal RNA-seq aligner. In *Bioinformatics* (Vol. 29, Issue 1, pp. 15–21). Oxford University Press (OUP). <https://doi.org/10.1093/bioinformatics/bts635>
  62. Patro, R., Duggal, G., Love, M. I., Irizarry, R. A., & Kingsford, C. (2017). Salmon provides fast and bias-aware quantification of transcript expression. In *Nature Methods* (Vol. 14,

- Issue 4, pp. 417–419). Springer Science and Business Media LLC. <https://doi.org/10.1038/nmeth.4197>
63. Genefu | Princess Margaret Bioinformatics and Computational Genomics Laboratory. Available online: <https://www.pmgenomics.ca/bhklab/software/genefu> (accessed on 26 June 2023).
  64. Hao, Y., Hao, S., Andersen-Nissen, E., Mauck, W. M., III, Zheng, S., Butler, A., Lee, M. J., Wilk, A. J., Darby, C., Zager, M., Hoffman, P., Stoeckius, M., Papalexi, E., Mimitou, E. P., Jain, J., Srivastava, A., Stuart, T., Fleming, L. M., Yeung, B., ... Satija, R. (2021). Integrated analysis of multimodal single-cell data. In *Cell* (Vol. 184, Issue 13, pp. 3573–3587.e29). Elsevier BV. <https://doi.org/10.1016/j.cell.2021.04.048>
  65. Gatz, M. L., Silva, G. O., Parker, J. S., Fan, C., & Perou, C. M. (2014). An integrated genomics approach identifies drivers of proliferation in luminal-subtype human breast cancer. In *Nature Genetics* (Vol. 46, Issue 10, pp. 1051–1059). Springer Science and Business Media LLC. <https://doi.org/10.1038/ng.3073>
  66. Smith, K. M., Fagan, P. C., Pomari, E., Germano, G., Frasson, C., Walsh, C., Silverman, I., Bonvini, P., & Li, G. (2018). Antitumor Activity of Entrectinib, a Pan-TRK, ROS1, and ALK Inhibitor, in ETV6-NTRK3–Positive Acute Myeloid Leukemia. In *Molecular Cancer Therapeutics* (Vol. 17, Issue 2, pp. 455–463). American Association for Cancer Research (AACR). <https://doi.org/10.1158/1535-7163.mct-17-0419>
  67. Xu, X., Wang, J., Han, K., Li, S., Xu, F., & Yang, Y. (2018). Antimalarial drug mefloquine inhibits nuclear factor kappa B signaling and induces apoptosis in colorectal cancer cells. In *Cancer Science* (Vol. 109, Issue 4, pp. 1220–1229). Wiley. <https://doi.org/10.1111/cas.13540>
  68. Sapi, J., Kovacs, L., Drexler, D. A., Kocsis, P., Gajari, D., & Sapi, Z. (2015). Tumor Volume Estimation and Quasi-Continuous Administration for Most Effective Bevacizumab Therapy. In F. Bertolini (Ed.), *PLOS ONE* (Vol. 10, Issue 11, p. e0142190). Public Library of Science (PLoS). <https://doi.org/10.1371/journal.pone.0142190>
  69. Abramoff, M. D., Magalhaes, P. J., & Ram, S. J. (2004). Image Processing with ImageJ. In *Biophotonics International*, 11(7), 36–42.
  70. Bhasin, M., Reinherz, E. L., & Reche, P. A. (2006). Recognition and Classification of Histones Using Support Vector Machine. In *Journal of Computational Biology* (Vol. 13, Issue 1, pp. 102–112). Mary Ann Liebert Inc. <https://doi.org/10.1089/cmb.2006.13.102>
  71. Singh, R. K., Liang, D., Gajjalaiahvari, U. R., Kabbaj, M.-H. M., Paik, J., & Gunjan, A. (2010). Excess histone levels mediate cytotoxicity via multiple mechanisms. In *Cell Cycle* (Vol. 9, Issue 20, pp. 4236–4244). Informa UK Limited. <https://doi.org/10.4161/cc.9.20.13636>
  72. Center for Drug Evaluation and Research. (2020). FDA approves selinexor for refractory or relapsed multiple myeloma. U.S. Food and Drug Administration. <https://www.fda.gov/drugs/resources-information-approved-drugs/fda-approves-selinexor-refractory-or-relapsed-multiple-myeloma>
  73. Nakayama, R., Zhang, Y.-X., Czaplinski, J. T., Anatone, A. J., Sicinska, E. T., Fletcher, J. A., Demetri, G. D., & Wagner, A. J. (2016). Preclinical activity of selinexor, an inhibitor

- of XPO1, in sarcoma. In *Oncotarget* (Vol. 7, Issue 13, pp. 16581–16592). Impact Journals, LLC. <https://doi.org/10.18632/oncotarget.7667>
74. Zhao, C., Yang, Z., Zhang, J., Li, O., Liu, S., Cai, C., Shu, Y., Pan, L., Gong, W., & Dong, P. (2022). Inhibition of XPO1 with KPT-330 induces autophagy-dependent apoptosis in gallbladder cancer by activating the p53/mTOR pathway. In *Journal of Translational Medicine* (Vol. 20, Issue 1). Springer Science and Business Media LLC. <https://doi.org/10.1186/s12967-022-03635-w>
  75. Novartis Pharmaceuticals (2009, March 18 - 2012, August 31). Everolimus in Combination With Exemestane in the Treatment of Postmenopausal Women With Estrogen Receptor Positive Locally Advanced or Metastatic Breast Cancer Who Are Refractory to Letrozole or Anastrozole (BOLERO-2). Identifier NCT00863655. <https://clinicaltrials.gov/ct2/show/NCT00863655>
  76. Huffman, T. A., Mothe-Satney, I., & Lawrence, J. C., Jr. (2002). Insulin-stimulated phosphorylation of lipin mediated by the mammalian target of rapamycin. In *Proceedings of the National Academy of Sciences* (Vol. 99, Issue 2, pp. 1047–1052). *Proceedings of the National Academy of Sciences*. <https://doi.org/10.1073/pnas.022634399>
  77. Alasker, A., Meskawi, M., Sun, M., Ismail, S., Hanna, N., Hansen, J., Tian, Z., Bianchi, M., Perrotte, P., & Karakiewicz, P. I. (2013). A contemporary update on rates and management of toxicities of targeted therapies for metastatic renal cell carcinoma. In *Cancer Treatment Reviews* (Vol. 39, Issue 4, pp. 388–401). Elsevier BV. <https://doi.org/10.1016/j.ctrv.2012.12.006>
  78. Muqbil, I., Aboukameel, A., Elloul, S., Carlson, R., Senapedis, W., Baloglu, E., Kauffman, M., Shacham, S., Bhutani, D., Zonder, J., Azmi, A. S., & Mohammad, R. M. (2016). Anti-tumor activity of selective inhibitor of nuclear export (SINE) compounds, is enhanced in non-Hodgkin lymphoma through combination with mTOR inhibitor and dexamethasone. In *Cancer Letters* (Vol. 383, Issue 2, pp. 309–317). Elsevier BV. <https://doi.org/10.1016/j.canlet.2016.09.016>
  79. T P, A. (2009). Pharmacogenomics: The Right Drug to the Right Person. In *Journal of Clinical Medicine Research*. Elmer Press, Inc. <https://doi.org/10.4021/jocmr2009.08.1255>
  80. Tamvakopoulos, C. S., Colwell, L. F., Barakat, K., Fenyk-Melody, J., Griffin, P. R., Nargund, R., Palucki, B., Sebhat, I., Shen, X., & Stearns, R. A. (2000). Determination of brain and plasma drug concentrations by liquid chromatography/tandem mass spectrometry. In *Rapid Communications in Mass Spectrometry* (Vol. 14, Issue 19, pp. 1729–1735). Wiley. [https://doi.org/10.1002/1097-0231\(20001015\)14:19<1729::aid-rcm85>3.0.co;2-5](https://doi.org/10.1002/1097-0231(20001015)14:19<1729::aid-rcm85>3.0.co;2-5)
  81. Anandharaj, A., Cinghu, S., & Park, W.-Y. (2011). Rapamycin-mediated mTOR inhibition attenuates survivin and sensitizes glioblastoma cells to radiation therapy. In *Acta Biochimica et Biophysica Sinica* (Vol. 43, Issue 4, pp. 292–300). China Science Publishing & Media Ltd. <https://doi.org/10.1093/abbs/gmr012>
  82. Lehmann, B. D., Colaprico, A., Silva, T. C., Chen, J., An, H., Ban, Y., Huang, H., Wang, L., James, J. L., Balko, J. M., Gonzalez-Ericsson, P. I., Sanders, M. E., Zhang, B., Pietenpol, J. A., & Chen, X. S. (2021). Multi-omics analysis identifies therapeutic vulnerabilities in

triple-negative breast cancer subtypes. In *Nature Communications* (Vol. 12, Issue 1). Springer Science and Business Media LLC. <https://doi.org/10.1038/s41467-021-26502-6>

## Appendix

### Supplementary Table 1: List of drugs of interest and genes encoding their drug target(s) compiled by Tia H. Turner.

Drugs chosen for synergism testing are bolded.

Drug	Gene(s)
<b>17-AAG (KOS953)</b>	HSP90AA1
ABT-263 (Navitoclax)	BCL2
Afatinib (BIBW2992)	EGFR
Aprotinin	PLG
AT13387 (Onalespib)	HSP90AA1
AZD-9291 (Osimertinib)	EGFR
<b>Azelnidipine</b>	CACNA1A, CACNA1B, CACNA1C, CACNA1D, CACNB1
Bardoxolone methyl	KEAP1
Bazedoxifene HCl	ESR1
<b>Belinostat (PXD101)</b>	Multiple HDACs
Candesartan Cilexetil	AGTR1
Cinacalcet HCl	CASR
Clomiphene citrate	ESR1
Dacomitinib (PF299804, PF299)	EGFR
Dronedarone	KCNA5
EMD-1214063	MET
<b>Entrectinib</b>	ALK, ROS1, NTRK1, NTRK2, NTRK3
Fingolimod (FTY720)	KCNJ5
Idarubicin HCl	TOP2A
LDK378	ALK
Lomerizine HCl	CACNA1B, CACNA1C, CACNA1A, CACNA1D, CACNA1H, CACNA1E
LY2835219	CDK4, CDK6
<b>Mefloquine hydrochloride</b>	N/A
Pacritinib	FLT3
PCI-24781 (CRA-024781)	HDAC1
Pozotinib	EGFR
Rapamycin (Sirolimus)	FKBP1A, MTOR
Sertraline HCl	SLC6A4
Tamoxifen Citrate	ESR1
Thioridazine HCl	HTR1A
Topotecan	TOP1
Vorinostat (SAHA, MK0683)	HDAC1
Vortioxetine (Lu AA21004) HBr	HTR1A
Ziprasidone hydrochloride monohydrate	HTR1A
<b>Selinexor (KPT-330)</b>	XPO1

**Supplementary Table 2: p-values for PDX KPT-330 dose response data shown in Figure 1B calculated by Tia H. Turner.**

Unpaired students *t* tests were performed to analyze differences in cell viability between vehicle and drug-treated conditions; p-values < 0.05 are bolded and italicized. N refers to the number of independent triplicate experiments.

<b>[KPT-330]</b> <b>(<math>\mu</math>M)</b>	<b>HCI-001</b> N=3	<b>UCD52</b> N=3	<b>WHIM2</b> N=3	<b>WHIM30</b> N=3
<b>0.001</b>	0.69507279	0.08897	<b><i>0.01218</i></b>	<b><i>0.031275</i></b>
<b>0.01</b>	0.65404176	<b><i>0.04721</i></b>	<b><i>0.017614</i></b>	<b><i>0.035125</i></b>
<b>0.1</b>	<b><i>0.00730741</i></b>	<b><i>0.001464</i></b>	<b><i>0.000684</i></b>	<b><i>0.012466</i></b>
<b>1</b>	<b><i>0.00116676</i></b>	<b><i>1.65E-06</i></b>	<b><i>0.003796</i></b>	<b><i>0.000181</i></b>
<b>10</b>	<b><i>0.00656469</i></b>	<b><i>9.86E-06</i></b>	<b><i>0.004377</i></b>	<b><i>5.14E-05</i></b>
<b>100</b>	<b><i>1.5924E-07</i></b>	<b><i>8.81E-08</i></b>	<b><i>2.14E-09</i></b>	<b><i>6.89E-08</i></b>

**Supplementary Table 3: Concentrations of drugs used in PDX dose response and synergism experiments shown in Figures 4-6 calculated by Tia H. Turner.**

<b>HCI-001</b>	<b>KPT-330</b>	<b>17-AAG</b>	<b>Azelnidipine</b>	<b>Belinostat</b>	<b>Entrectinib</b>	<b>Mefloquine</b>
Dose 1 (μM)	0.109375	0.015625	0.109375	0.03125	0.109375	0.046875
Dose 2 (μM)	0.4375	0.0625	0.4375	0.125	0.4375	0.1875
Dose 3 (μM)	1.75	0.25	1.75	0.5	1.75	0.75
Dose 4 (μM)	7	1	7	2	7	3
Dose 5 (μM)	28	4	28	8	28	12
Dose 6 (μM)	112	16	112	32	112	48
Dose 7 (μM)	448	64	448	128	448	192
<b>UCD52</b>	<b>KPT-330</b>	<b>17-AAG</b>	<b>Azelnidipine</b>	<b>Belinostat</b>	<b>Entrectinib</b>	<b>Mefloquine</b>
Dose 1 (μM)	0.009375	0.001563	0.0625	0.03125	0.0625	0.0625
Dose 2 (μM)	0.0375	0.00625	0.25	0.125	0.25	0.25
Dose 3 (μM)	0.15	0.025	1	0.5	1	1
Dose 4 (μM)	0.6	0.1	4	2	4	4
Dose 5 (μM)	2.4	0.4	16	8	16	16
Dose 6 (μM)	9.6	1.6	64	32	64	64
Dose 7 (μM)	38.4	6.4	256	128	256	256
<b>WHIM2</b>	<b>KPT-330</b>	<b>17-AAG</b>	<b>Azelnidipine</b>	<b>Belinostat</b>	<b>Entrectinib</b>	<b>Mefloquine</b>
Dose 1 (μM)	0.078125	0.03125	0.019531	0.001953	0.027344	0.015625
Dose 2 (μM)	0.3125	0.125	0.078125	0.007813	0.109375	0.0625
Dose 3 (μM)	1.25	0.5	0.3125	0.03125	0.4375	0.25
Dose 4 (μM)	5	2	1.25	0.125	1.75	1
Dose 5 (μM)	20	8	5	0.5	7	4
Dose 6 (μM)	80	32	20	2	28	16
Dose 7 (μM)	320	128	80	8	112	64
<b>WHIM30</b>	<b>KPT-330</b>	<b>17-AAG</b>	<b>Azelnidipine</b>	<b>Belinostat</b>	<b>Entrectinib</b>	<b>Mefloquine</b>
Dose 1 (μM)	0.015625	0.078125	0.078125	0.03125	0.109375	0.078125
Dose 2 (μM)	0.0625	0.3125	0.3125	0.125	0.4375	0.3125
Dose 3 (μM)	0.25	1.25	1.25	0.5	1.75	1.25
Dose 4 (μM)	1	5	5	2	7	5
Dose 5 (μM)	4	20	20	8	28	20
Dose 6 (μM)	16	80	80	32	112	80
Dose 7 (μM)	64	320	320	128	448	320

**Supplementary Table 4: p-values for dose response data shown in Figure 4 calculated by Tia H. Turner.**

Unpaired students *t* tests were performed to analyze differences in cell viability between vehicle and drug-treated conditions; p-values < 0.05 are bolded and italicized.

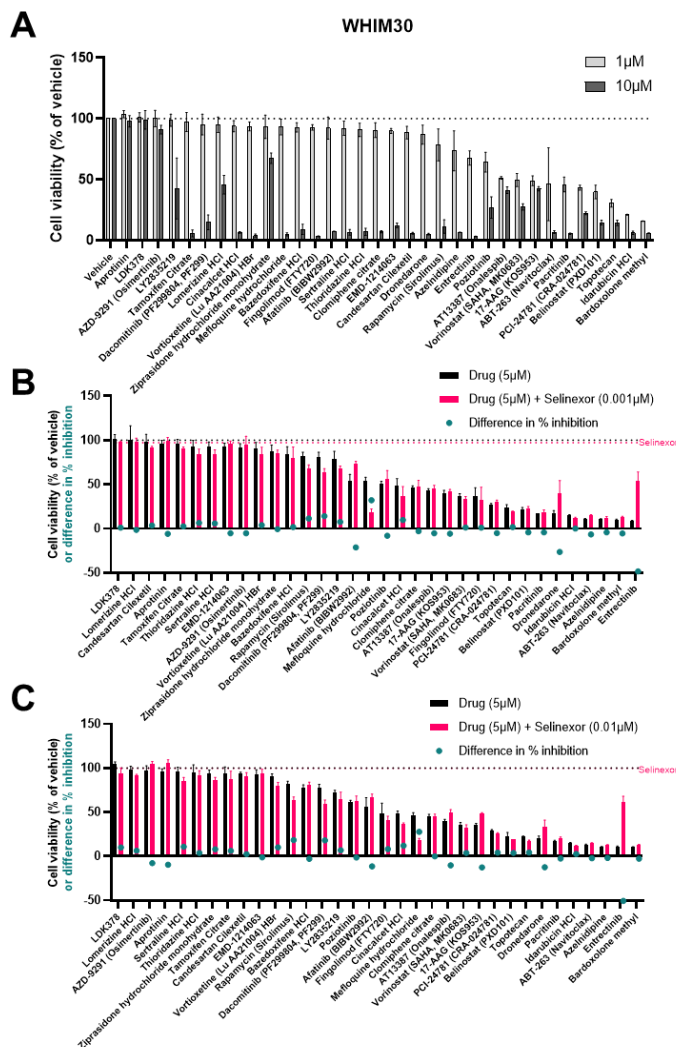
<b>KPT-330</b>	<b>HCI-001</b>	<b>UCD52</b>	<b>WHIM2</b>	<b>WHIM30</b>	<b>Belinostat</b>	<b>HCI-001</b>	<b>UCD52</b>	<b>WHIM2</b>	<b>WHIM30</b>
Dose 1	<i>2.65E-08</i>	<i>1.49E-21</i>	<i>2.76E-07</i>	<i>0.000618</i>	Dose 1	0.169462	<i>0.014201</i>	0.529103	<i>0.00444</i>
Dose 2	<i>4.83E-08</i>	<i>4.84E-17</i>	<i>9.12E-07</i>	<i>1.11E-08</i>	Dose 2	<i>0.017768</i>	<i>0.016169</i>	0.137722	<i>0.000417</i>
Dose 3	<i>2.88E-10</i>	<i>1.32E-18</i>	<i>7.8E-11</i>	<i>7.28E-14</i>	Dose 3	<i>0.005145</i>	<i>0.025384</i>	<i>0.046157</i>	<i>0.008838</i>
Dose 4	<i>8E-13</i>	<i>8.87E-21</i>	<i>1.57E-14</i>	<i>2.6E-16</i>	Dose 4	<i>0.00234</i>	<i>0.003629</i>	<i>0.001544</i>	<i>0.005671</i>
Dose 5	<i>7.79E-18</i>	<i>1.14E-24</i>	<i>4.59E-15</i>	<i>6.37E-21</i>	Dose 5	<i>0.00122</i>	<i>0.000296</i>	<i>0.000117</i>	<i>0.011937</i>
Dose 6	<i>1.23E-31</i>	<i>7.4E-28</i>	<i>2.13E-36</i>	<i>1.07E-22</i>	Dose 6	<i>0.000231</i>	<i>3.16E-05</i>	<i>7.09E-06</i>	<i>0.003728</i>
Dose 7	<i>7.99E-37</i>	<i>5.06E-34</i>	<i>1.5E-44</i>	<i>3.08E-35</i>	Dose 7	<i>1.34E-05</i>	<i>2.17E-06</i>	<i>5.09E-09</i>	<i>0.000152</i>
<b>17-AAG</b>	<b>HCI-001</b>	<b>UCD52</b>	<b>WHIM2</b>	<b>WHIM30</b>	<b>Entrectinib</b>	<b>HCI-001</b>	<b>UCD52</b>	<b>WHIM2</b>	<b>WHIM30</b>
Dose 1	<i>0.031405</i>	0.15945	0.069221	0.392127	Dose 1	<i>0.000436</i>	<i>5.1E-06</i>	0.45278	0.424082
Dose 2	<i>0.029577</i>	0.615338	<i>0.002882</i>	<i>0.02613</i>	Dose 2	<i>0.014592</i>	0.147971	0.226504	0.889985
Dose 3	<i>0.017308</i>	<i>0.005012</i>	<i>0.001756</i>	0.161931	Dose 3	<i>0.020677</i>	0.212155	0.432073	<i>0.000519</i>
Dose 4	<i>0.025374</i>	<i>0.000846</i>	<i>0.00561</i>	0.062854	Dose 4	0.155966	0.05313	<i>0.003097</i>	0.269426
Dose 5	<i>0.021065</i>	<i>0.000183</i>	<i>0.003664</i>	<i>0.000737</i>	Dose 5	<i>0.000124</i>	<i>0.000107</i>	<i>0.000241</i>	0.297705
Dose 6	<i>0.012853</i>	<i>1.69E-05</i>	<i>6.86E-05</i>	<i>0.042784</i>	Dose 6	<i>2.61E-06</i>	<i>3.78E-06</i>	<i>3E-06</i>	<i>5.38E-05</i>
Dose 7	<i>0.000196</i>	<i>6.78E-06</i>	<i>0.004478</i>	<i>0.001536</i>	Dose 7	<i>2.37E-07</i>	<i>4.17E-07</i>	<i>7.96E-06</i>	<i>1.91E-05</i>
<b>Azelmidipine</b>	<b>HCI-001</b>	<b>UCD52</b>	<b>WHIM2</b>	<b>WHIM30</b>	<b>Mefloquine</b>	<b>HCI-001</b>	<b>UCD52</b>	<b>WHIM2</b>	<b>WHIM30</b>
Dose 1	0.094944	0.719205	0.486096	0.197954	Dose 1	<i>0.000231</i>	0.13871	<i>0.013083</i>	0.309928
Dose 2	0.303472	0.625839	0.110149	0.980041	Dose 2	<i>0.022977</i>	0.062358	0.142021	0.570796
Dose 3	<i>0.000363</i>	0.581185	0.708718	0.261562	Dose 3	<i>0.03959</i>	<i>0.014806</i>	0.247862	<i>0.010296</i>
Dose 4	<i>0.001251</i>	<i>0.044047</i>	<i>0.018401</i>	<i>5.58E-07</i>	Dose 4	<i>0.028841</i>	<i>0.00938</i>	0.651005	<i>0.004689</i>
Dose 5	<i>8.99E-06</i>	<i>7.44E-05</i>	<i>4.69E-06</i>	<i>6.63E-05</i>	Dose 5	<i>4.35E-06</i>	<i>1E-05</i>	0.090238	<i>0.026051</i>
Dose 6	<i>1.75E-06</i>	<i>1.72E-06</i>	<i>3.02E-06</i>	<i>1.34E-05</i>	Dose 6	<i>7.13E-07</i>	<i>6.1E-07</i>	<i>5.86E-06</i>	<i>2.91E-05</i>
Dose 7	<i>1.63E-06</i>	<i>6.78E-06</i>	<i>7.55E-07</i>	<i>1.4E-05</i>	Dose 7	<i>3.79E-10</i>	<i>9.16E-07</i>	<i>1.33E-09</i>	<i>1.92E-05</i>



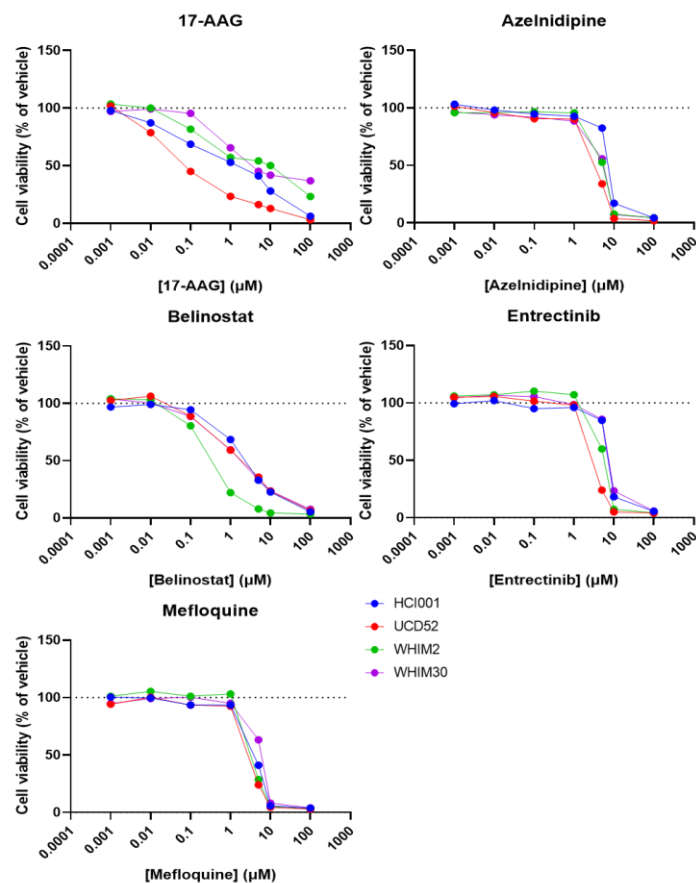




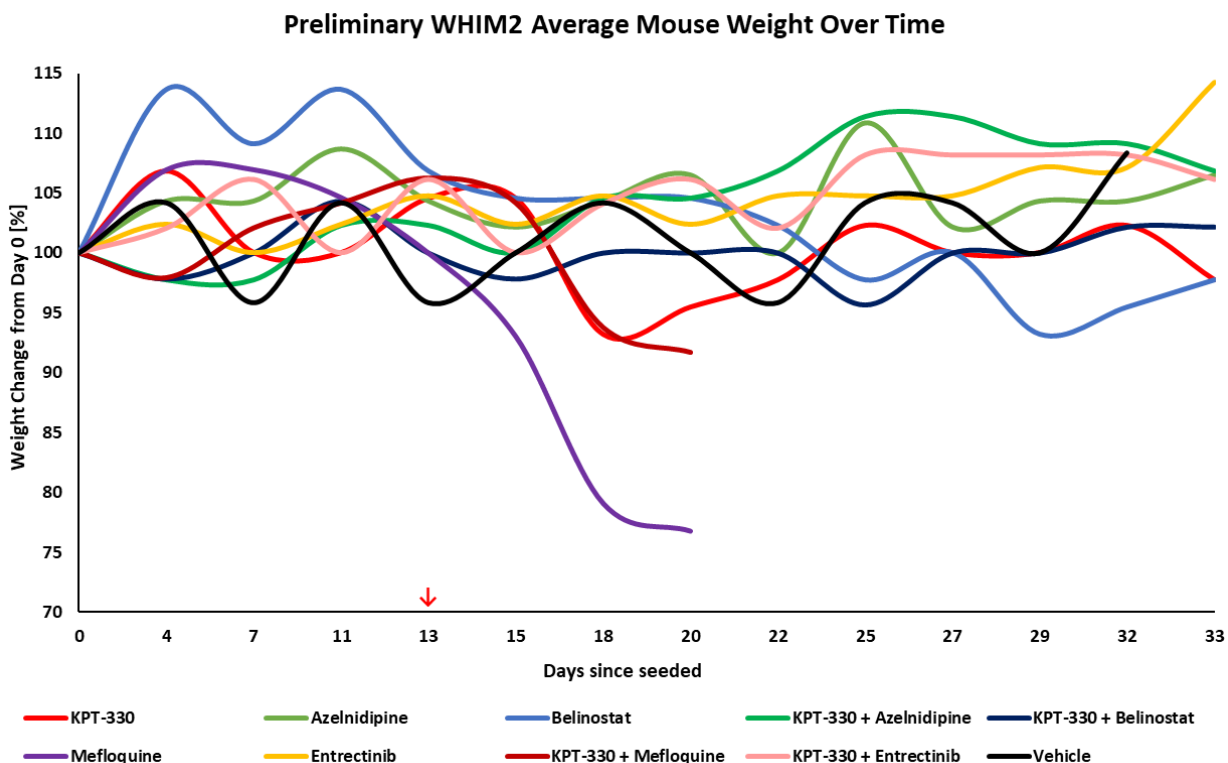




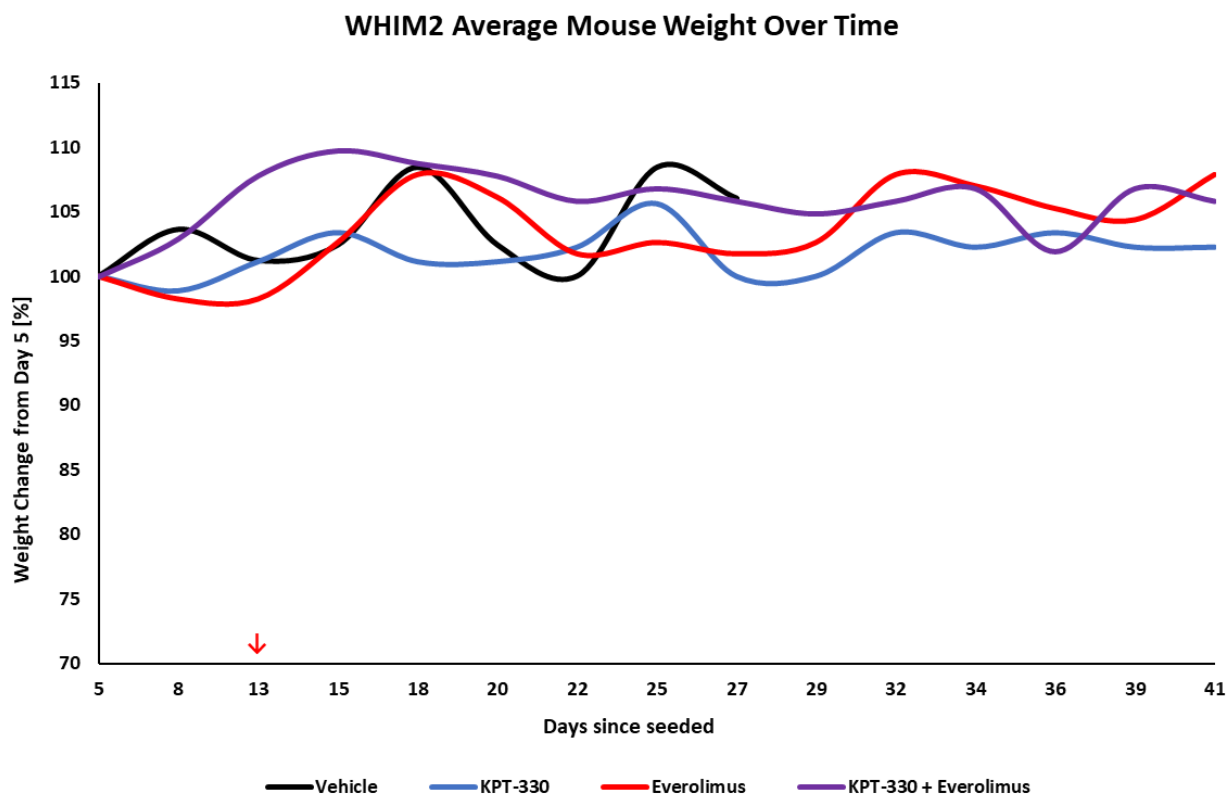
**Supplementary Figure 4: *In vitro* efficacy of 34 drugs alone and combined with KPT-330 in WHIM30 PDX cells assessed by Tia H. Turner.** (A) Cell viability (percent of vehicle) in response to 34 blood-brain barrier permeable drugs at 1 and 10  $\mu\text{M}$ . One independent experiment was performed in quadruplicates; error bars represent standard deviation across quadruplicates. (B-C) Graphs depict cell viability (percent of vehicle) in response to 34 drugs at 5  $\mu\text{M}$  alone (black bars) and in combination with KPT-330 (pink bars) at 0.001  $\mu\text{M}$  (B) or 0.01  $\mu\text{M}$  (C). KPT-330 alone is represented by a pink dotted line. Blue dots represent the difference in percent inhibition between each drug alone and in combination; the difference in percent inhibition  $>0$  suggests supra-additivity, 0 suggests additivity, and  $<0$  suggests sub-additivity. One independent experiment was performed in triplicates for each dose of KPT-330; error bars represent standard deviation across triplicates.



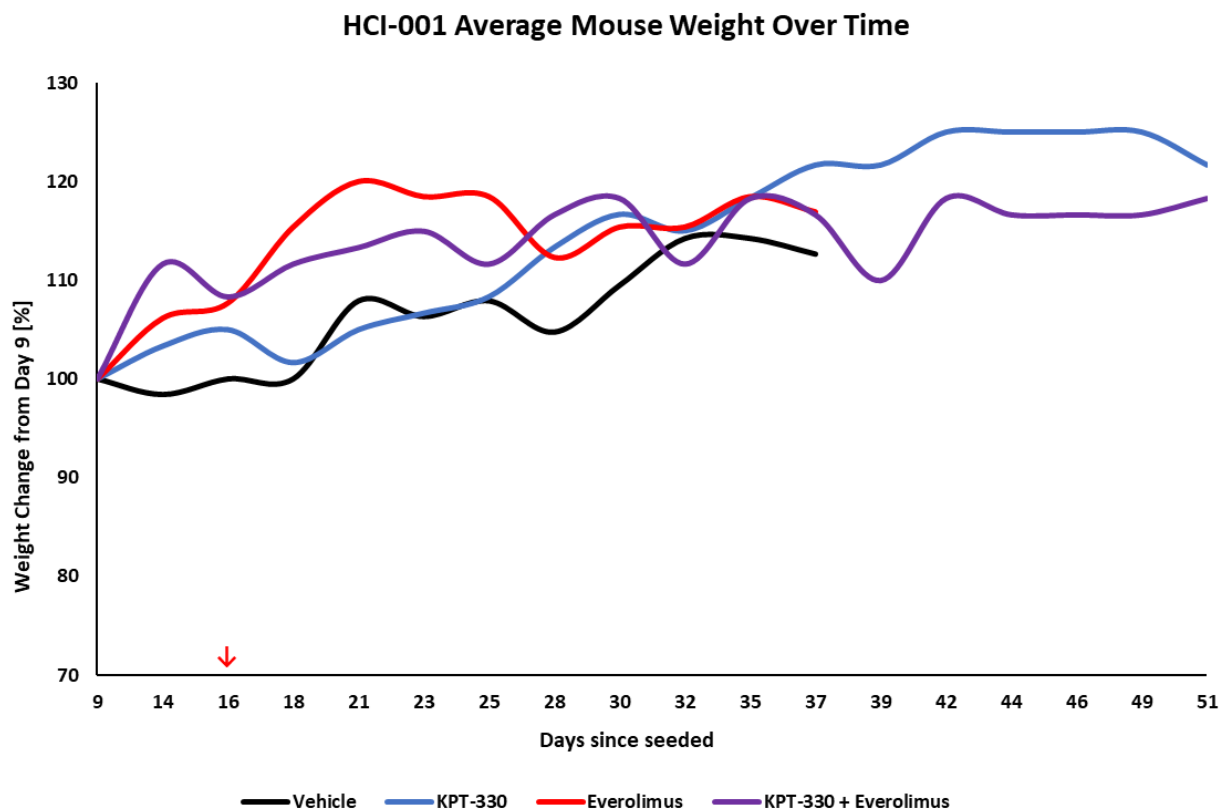
**Supplementary Figure 5: Dose-response curves for five drugs of interest in basal-like TNBC PDXs conducted by Tia H. Turner.** Graphs depict the viability (percent of vehicle) of PDX cells (HCI-001, UCD52, WHIM2, WHIM30) in response to increasing concentrations of the indicated drugs. One independent experiment was performed in triplicate for each PDX.



**Supplementary Figure 6: Preliminary *in vivo* study average mouse weights.** *In vivo* average mouse weight change since day 0 (first weight measurement, %) after treatment with vehicle (black), KPT-330 (red), Mefloquine (purple), Azelnidipine (light green), Entrectinib (yellow), Belinostat (blue), KPT-330 + Mefloquine (brown), KPT-330 + Azelnidipine (dark green), KPT-330 + Entrectinib (orange) and KPT-330 + Belinostat (indigo), with  $n = 2$  per group. Treatments started on day 13 since seeded (red arrow).

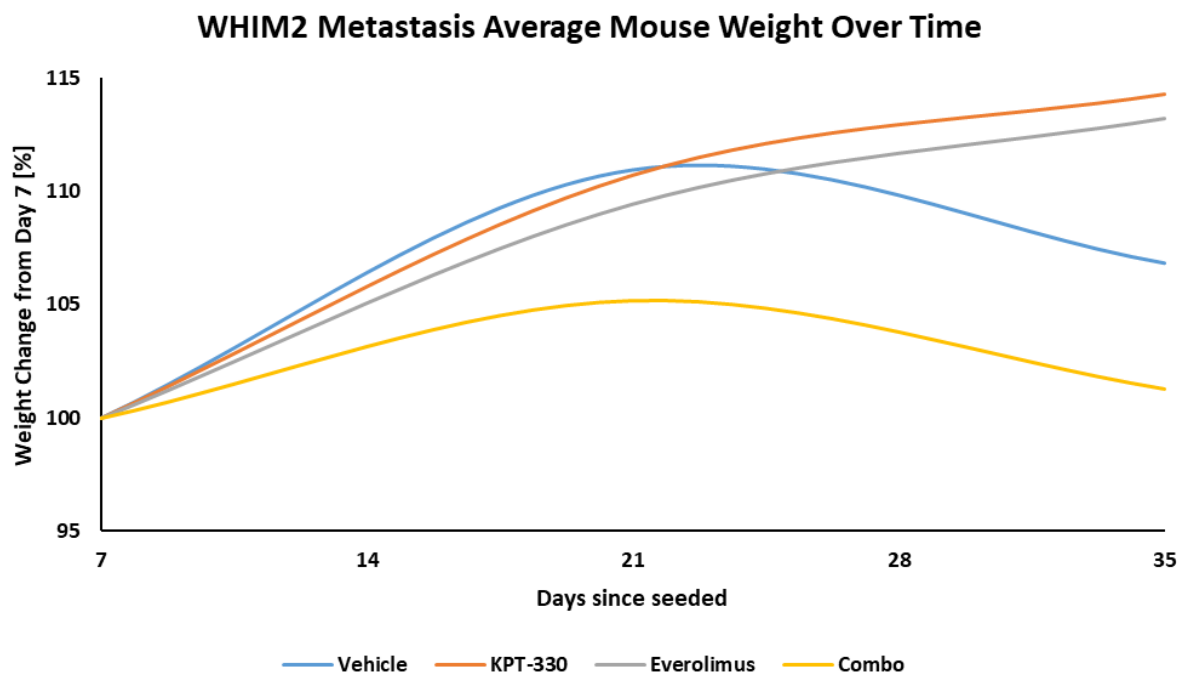


**Supplementary Figure 7: WHIM2 *in vivo* study average mouse weights.** *In vivo* average mouse weight change since day 5 (first weight measurement, %) after treatment with vehicle (black, n = 4), KPT-330 (blue, n = 4), everolimus (red, n = 5) or KPT-330 + everolimus (purple, n = 5). Treatments started on day 13 since seeded (red arrow).

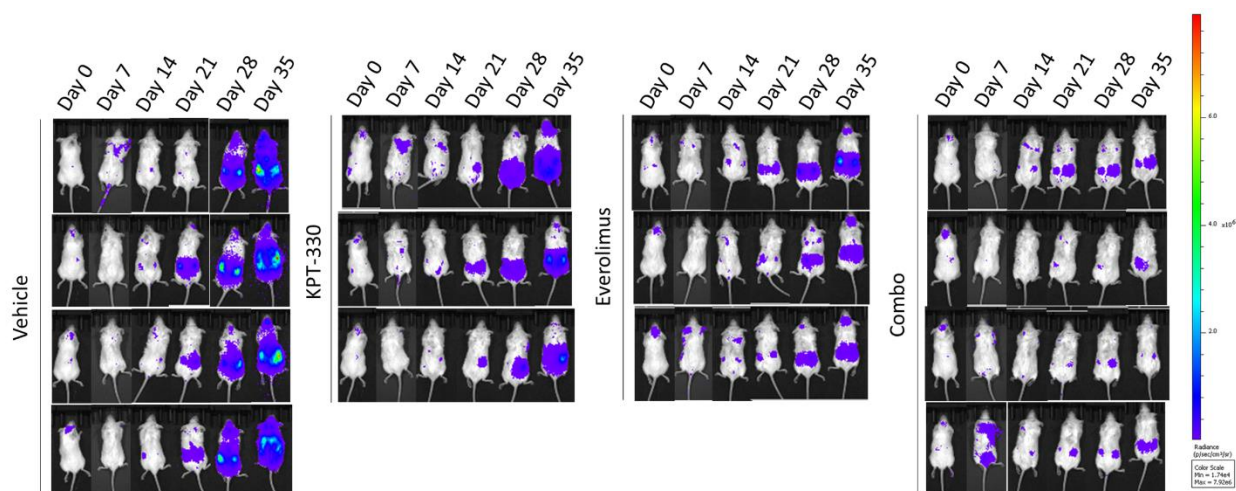


**Supplementary Figure 8: HCI-001 *in vivo* study average mouse weights.** *In vivo* average mouse weight change since day 9 (first weight measurement, %) after treatment with vehicle (black), KPT-330 (blue), everolimus (red), or KPT-330 + everolimus (purple), with n = 3 per group. Treatments started on day 16 since seeded (red arrow).





**Supplementary Figure 9: Metastasis *in vivo* study mouse weights.** *In vivo* average mouse weight change since day 7 (first weight measurement, %) after treatment with vehicle (blue, n = 4), KPT-330 (orange, n = 3), everolimus (grey, n = 3) or KPT-330 + everolimus (yellow, n = 4). Treatments started on day 8 since seeded.



**Supplementary Figure 10: Total metastasis spread over time.** IVIS images of luciferin-cleaved radiance (p/sec/cm<sup>2</sup>/sr) in NSG mice burdened with WHIM2 metastasis from day 0 through day 35. Mice were treated either with vehicle (n = 4), KPT-330 (n = 3), everolimus (n = 3) or Combo (n = 4). A radiance scalebar next to the images depicts radiance intensity, with red depicting the highest radiance and purple depicting the lowest radiance.

## Vita

Aaron David Valentine was born on December 21, 1999 in San Antonio TX, USA. He attended Gymnasium Goch in North Rhine-Westphalia, Germany from 2010 – 2014, then O’Fallon Township High School in O’Fallon IL, USA from 2014 – 2016, and then subsequently Ramstein High School in Ramstein AFB, Germany from 2016 – 2018 where he received his High School Diploma. Then, he attended Jacobs University Bremen in Bremen, Germany from 2018 – 2021, where he received his Bachelor of Science in Biochemistry and Cell Biology with a minor in Medicinal Chemistry and Chemical Biology. In the Brix Lab Group, he finished his BS Project & Thesis titled *SARS-CoV-2 Spike Protein Interaction with Human Thyroid Cells*. Afterwards, he attended Virginia Commonwealth University from 2021 – 2023 and graduated with a Master of Science in Biology.

**Valentine, A.** (2023, May 2). COMPASS Outreach Grants and Why You Should Apply. ASCB Newsletter, 46, 9.

Dozmorov, M. G., Marshall, M. A., Rashid, N. S., Grible, J. M., **Valentine, A.**, Olex, A. L., Murthy, K., Chakraborty, A., Reyna, J., Figueroa, D. S., Hinojosa-Gonzalez, L., Da-Inn Lee, E., Baur, B. A., Roy, S., Ay, F., & Harrell, J. C. (2023). Rewiring of the 3D genome during acquisition of carboplatin resistance in a triple-negative breast cancer patient-derived xenograft. In *Scientific Reports* (Vol. 13, Issue 1). Springer Science and Business Media LLC. <https://doi.org/10.1038/s41598-023-32568-7>

Boyd, D. C., Zboril, E. K., Olex, A. L., Leftwich, T. J., Hairr, N. S., Byers, H. A., **Valentine, A. D.**, Altman, J. E., Alzubi, M. A., Grible, J. M., Turner, S. A., Ferreira-Gonzalez, A., Dozmorov, M. G., & Harrell, J. C. (2023). Discovering Synergistic Compounds with BYL-719 in PI3K Overactivated Basal-like PDXs. In *Cancers* (Vol. 15, Issue 5, p. 1582). MDPI AG. <https://doi.org/10.3390/cancers15051582>

Dozmorov, M., Marshall, M., Rashid, N., Grible, J., **Valentine, A. D.**, Olex, A., Murthy, K., Chakraborty, A., Reyna, J., Figueroa, D. S., Lee, D.-I., Baur, B., Roy, S., Ay, F., & Harrell, J. C. (2023). Abstract P1-13-23: Carboplatin resistance-associated changes in the 3D chromatin landscape of a triple-negative breast cancer Patient-Derived Xenograft. In *Cancer Research* (Vol. 83, Issue 5\_Supplement, pp. P1-13-23-P1-13-23). American Association for Cancer Research (AACR). <https://doi.org/10.1158/1538-7445.sabcs22-p1-13-23>

**Valentine, A. D.**, Turner, T. H., Rashid, N. S., Hairr, N. S., Leftwich, T. J., Harrell, J. C. (2022). Identification of Synergistic Therapeutics for Basal-like Breast Cancer Brain Metastases. *Mol Biol Cell* 34, B254/P1936. Part of <https://doi.org/10.1091/mbc.E22-12-0555>

Rashid, N. S., Boyd, D. C., Olex, A. L., Grible, J. M., Duong, A. K., Alzubi, M. A., Altman, J. E., Leftwich, T. J., **Valentine, A. D.**, Hairr, N. S., Zboril, E. K., Smith, T. M., Jr., Pfefferle, A. D., Dozmorov, M. G., & Harrell, J. C. (2022). Transcriptomic changes underlying EGFR inhibitor resistance in human and mouse models of basal-like breast cancer. In *Scientific Reports* (Vol. 12, Issue 1). Springer Science and Business Media LLC. <https://doi.org/10.1038/s41598-022-25541-3>

Pedersen, R., **Valentine, A.**, Coté, L. (2022, October 25). Dear mentors, remember lingering pandemic impacts on trainees. ASCB Newsletter, 45, 26-28.

**Valentine, A. D.**, Rehders, M., Brix, K. (2021). Generation of a ciliogenesis model in human thyroid cells. Mol Biol Cell 32, P347. Part of <https://doi.org/10.1091/mbc.E21-11-0545>

Qatato, M., Venugopalan, V., Al-Hashimi, A., Rehders, M., **Valentine, A. D.**, Hein, Z., Dallto, U., Springer, S., & Brix, K. (2021). Trace Amine-Associated Receptor 1 Trafficking to Cilia of Thyroid Epithelial Cells. In Cells (Vol. 10, Issue 6, p. 1518). MDPI AG. <https://doi.org/10.3390/cells10061518>